# LOPSIDEDNESS IN DWARF IRREGULAR GALAXIES

Ana B. Heller, Noah Brosch, Elchanan Almoznino

The Wise Observatory and the School of Physics and Astronomy

Tel Aviv University, Tel Aviv 69978, Israel.

Liese van Zee

Herzberg Institute of Astrophysics

5071 W. Saanich Rd., Victoria BC V8X 4M6, Canada.

and

John J. Salzer

Astronomy Department, Wesleyan University,

Middletown, CT 06459-0123.

Received _____; accepted _____

## ABSTRACT

We quantify the amplitude of the lopsidedness, the azimuthal angular asymmetry index, and the concentration of star forming regions, as represented by the distribution of the H$\alpha$ emission, in a sample of 78 late-type irregular galaxies. We bin the observed galaxies in two groups representing blue compact galaxies (BCDs) and low surface brightness dwarf galaxies (LSBs). The light distribution is analysed with a novel algorithm, which allows detection of details in the light distribution pattern. We find that while the asymmetry of the underlying continuum light, representing the older stellar generations, is relatively small, the H$\alpha$ emission is very asymmetric and is correlated in position angle with the continuum light. We show that the concentration of continuum light is correlated with the H$\alpha$ concentration; this implies that the young star formation has the same spatial properties as the older stellar populations, but that these properties are more strongly expressed by the young stars. We test a model of random star formation over the extent of a galaxy by simulating HII regions in artificial dwarf galaxies. A galaxy is traced by assuming red star clusters distributed on an underlying exponential disk of radius twice the scale length. The disk is allowed to change in apparent magnitude, scale radius, position angle, and ellipticity. We compare the asymmetry-concentration distribution predicted by the simulations with the real observed distribution; we find that only LSBs match the distribution predicted by the model. The reason is that, independently of the number of HII regions, LSBs show no particular location of HII regions, whereas BCDs show current star formation activity restricted very much to the central parts of the galaxies. A consideration of the properties of the continuum light leads to the conclusion that most

of LSBs can be approximated by exponential disks of radius twice their scale lengths; BCDs call, however, for much more concentrated underlying systems, with smaller scale lengths than assumed in the simulations. The implication is that random star formation over the full extent of a galaxy may be generated in LSB dwarf-irregular galaxies but not in BCD galaxies.

Keywords: lopsidedness, HII regions, late-type galaxies

## 1. Introduction

One of the least understood aspects of galaxy evolution is the onset of lopsidedness in the gaseous and stellar distributions of disk galaxies. Recent models of disk galaxies suggest that the presence of a dominant dark halo can both produce and help sustain asymmetries in the gaseous and stellar components. For instance, a lopsided gravitational potential of a dark matter halo can produce an asymmetric galaxy as the gas surface density responds to the overall asymmetry (Jog 1997). Alternatively, a symmetric dark matter halo can produce an asymmetric galaxy if the disk orbits off–center of the overall potential (Levine & Sparke 1998). In addition to these "intrinsic" models, the environment and merger history of a galaxy can affect its present appearance. For example, recent dynamical simulations of the effect of an infalling satellite indicate that tidal interactions are yet another mechanism by which asymmetric galaxies can be formed (Walker, Mihos, & Hernquist 1996; Zaritsky & Rix 1997).

However, all the above models were designed to account for asymmetries observed in massive spiral galaxies. The question of asymmetries in dwarf irregular galaxies (dIs) may demand a different approach, as dIs lack spiral density waves and tidal shear forces that contribute to induce gas instabilities. In dIs, the gas appears to be close to stability throughout the disk, even though star formation is occurring (Hunter *et al.* 1998). Moreover, there is growing evidence (Mihos, McGaugh & de Blok 1997) that low-surface-brightness (LSB) disks are reasonably stable and remain structurally intact during tidal encounters. In addition, various tests of Virgo dIs favor internal over external mechanisms of star formation (Heller *et al.* 1998), with the implicit conclusion that asymmetries may also form through internal mechanisms.

We conclude that, while theoretical arguments, such as the presence of a dominant dark matter halo potential in dIs, may contribute to the long-persistence of the asymmetries, other processes of star formation, such as the Stochastic Self-Propagating

Star Formation (SSPSF, Gerola, Seiden & Schulman 1980), or alternatively random gas compression from turbulence, or random collisions of ISM clouds (Larson 1986; Elmegreen 1998) may be the dominant regulators of the star formation in dIs. This conclusion is supported by recent star formation histories (SFH) of Sextans A and GR 8 derived from HST observations. A series of chronological frames showing the spatial distribution of blue HeB stars indicate that, chronologically, the star formation activity is propagating around in these galaxies with typical sizes of ∼100 pc and lifetimes of order 100 Myr (Dohm-Palmer *et al.* 1997, 1998a, b). The question remains as to whether random mechanisms may introduce temporary asymmetries in the stellar and gaseous components of low-mass systems. We address this issue by (a) analyzing the light distribution in deep narrow-band H$\alpha$ and continuum images of a large sample of star forming dIs, (b) developing a new impartial algorithm to compute the lopsidedness of star-forming regions and simultaneously compare it to the distribution of the stellar component, (c) constructing 1000 model galaxies and showing that it is the "discrete" behavior of random star forming regions that produce the asymmetric structure observed in most of the dIs.

The plan of the paper is as follows: we first describe the sample of galaxies, which is a collection of objects with previously published observations. The analysis method is described next, then the results are presented. Finally, we describe the simulations performed to understand the observational results and their implications.

## 2. The sample

The galaxy sample studied here consists of 78 dIs observed with the Wise Observatory (WO) 1.0 m telescope or with the Kitt Peak National Observatory (KPNO) 0.9 m telescope. The galaxies are classified in the original publications as dIs, with absolute blue magnitudes < -18, and are smaller than 2 arcmin. The only restrictions

to the inclusion in the sample are the availability of CCD H$\alpha$ images with detected HII regions, and $v_\odot \leq 3,000$ km sec$^{-1}$ (except for UM408, which has $v_\odot = 3,492$ km sec$^{-1}$). All the selected galaxies appear to be isolated, with the exception of objects marked with an asterisk in Table 1. Representative H$\alpha$ images, catalog references, and extensive additional details, can be found in van Zee *et al.* (1997a, b, c), Almoznino & Brosch (1998), Heller *et al.* (1999, 2000), and Norton & Salzer (2000).

In order to test for dependence of the SFR on the lopsidedness we divided the sample in two sub-groups. The first, called here BCD, is represented by 33 blue compact dwarf galaxies (classified morphologically as BCD or anything+BCD: references 5, 6, and 7 in Table 1). These are galaxies whose optical light output is often dominated by the strong starburst component. The second group, called LSB, is represented by 45 low surface brightness dwarf galaxies (references 1, 2, 3, and 4). This group includes dIs, primarily from standard catalogues, which are gas-rich and, in general, have central surface brightness fainter than $\sim$ 23.0 mag arcsec$^{-2}$. Some of the more luminous LSB galaxies show evidence of spiral features and may belong to the "dwarf spiral" class (UGC numbers 191, 634, 3050, 3174, 4660, 5716, 7178, 9762, 10281, and 11820). The typical SFR for the LSB group is $\sim 7 \times 10^{-3}$ M$_\odot$ yr$^{-1}$; this is, on average, one order of magnitude weaker than for BCD objects, although there is overlap in SFR between the brighter LSBs and the fainter BCDs.

## 3. Analysis and results

### 3.1. Method

In general, the lopsidedness of a galaxy is measured on a broad-band image (usually in the red). Some authors (Zaritsky & Rix 1997; Rudnick & Rix 1998) use the ratio of the m=1 to m=0 Fourier amplitudes of the image as a quantitative measure of

lopsidedness in early-type disk galaxies. Others take a more direct approach of comparing the integrated light within specified regions of the galaxy. For instance, Kornreich *et al.* (1998) compare the relative fluxes within trapezoidal sectors arranged symmetrically about the galaxy's center of light. Similarly, Abraham *et al.* (1996) define the rotational asymmetry parameter as half the ratio of the absolute value of the difference between the original galaxy image and the image rotated by a half-turn about its center, to the original image. The rotational asymmetry parameter, together with the central concentration of the emitted flux, has proven to be an important tool to extend the morphological classification of the galaxies from the nearby Universe to high redshifts. Likewise, color-asymmetry diagrams, when combined with information about the axial ratio, can be used to disentangle interacting galaxies from non-interacting, face-on systems at high redshift (Conselice 1997; Conselice & Bershady 1999).

We have developed a new method to evaluate the variation of asymmetry with azimuthal position angle, and also the concentration of the star forming regions and of the general stellar distribution. In our method, the H$\alpha$ line emission represents the distribution of the recently formed massive stars that are younger than a few tens of Myrs, while the red continuum emission represents the distribution of the integrated stellar populations. This latter component may be contaminated by nebular continuum emission from HII regions, but nebular emission amounts to only 30% of the light during the first few Myrs of a starburst, and becomes negligible as soon as the first red supergiants appear, at about $10^{6.9}$ yr (Leitherer & Heckman 1995). We investigate both the asymmetry and concentration properties of these two components, as well as look for correlations between them.

For most galaxies in the sample, two red, narrow-band images were used: one centered on the rest-frame H$\alpha$ line ($H\alpha_{on}$) and the other sampling the continuum ($Cont$) region near H$\alpha$. For some of the LSBs, the narrow-band continuum images were no

longer available at the time of the present analysis. For these systems (marked "+" in Table 1), sky-subtracted B broad-band images were only used to trace the ellipse contour of the galaxies (see below) but are not included in the statistical results for *Cont*. In all cases, the sky background was subtracted in each band and the net-H$\alpha$ ($H\alpha$) images were derived by subtracting *Cont* from $H\alpha_{on}$ images with proper scaling. Details are given in Heller *et al.* (1999).

Due to the lack of obvious central concentration and the irregular shape of the galaxies, we performed different fits of elliptical isophotes, allowing the ellipticity and the position angle to vary, and fitting out to 25 mag arcsec$^{-2}$ on the continuum image. The convergence criterion for the final parameters was set when the outer isophote retained the position angle and ellipticity of the ellipse traced at half the major axis. From then on, the position angle, the ellipticity, and the extent of the galaxy were held fixed, and the outer ellipse contour was transposed to the H$\alpha$ images. For those objects without calibrated images, (refs. 2, 5, and 6 in Table 1), the outermost isophote was adopted at the level where the mean intensity reached the sky fluctuations. This choice presumably depends on the depth of the exposure and on systematic errors in the subtraction of the sky background. The reduction was done with IRAF[1] and the fitted ellipse parameters are listed in Table 1.

We integrated the fluxes in the two halves of the galaxy separated by a bisector line, represented by the major-axis of the outer ellipse, and computed the ratio of the lower flux to the higher flux from the two galaxy halves. The resulting ratio defines one asymmetry index (AI$_i$). After this, using the maximum allowed 90 vertexes of the ellipse contour produced from the ELLIPSE task of IRAF in the plane of the galaxy, we rotated the bisector anti-clockwise around the center of the ellipse to the line defined by the next two opposite vertexes, and thus obtained 90 asymmetry indices, one for each position

[1]IRAF is distributed by the National Optical Astronomy Observatories.

angle $\Phi_i$ of the vertex. For the maximum ellipticity (e=0.75) measured in the sample, we reach an upper spatial resolution of $\Phi_i$= 0.4 degrees, and a lower resolution of $\Phi_i$=4.4 degrees. For example, in a perfect circle (ellipticity e=0) the resolution is $\Phi_i = 4$ degrees. This method is more useful than the usual one constructed from two asymmetry indices because it covers the full range of possibilities in azimuthal angle. Moreover, the presence of faint HII regions is emphasized by the irregularities in the luminosity profiles. The variation of AI with position angle (the "lopsidedness distribution", LD) is plotted for each galaxy in the sample in Figures 1.1 to 2.3.

A representative lopsidedness index (A) for each galaxy was computed by normalizing the total lopsidedness range (the difference between maximum and minimum AI) to the maximum asymmetry index: $A = \frac{AI_{max} - AI_{min}}{AI_{max}}$. The mean asymmetry index <AI>, the lopsidedness index (A), and the asymmetry amplitude $ampl = \frac{AI_{max} - AI_{min}}{2}$ are listed in Tables 2.1, 2.2, and 2.3. A symmetric distribution of the light is represented by A=0 and $AI_{max}$=1, while an extremely asymmetric distribution will have A=1 and $AI_{min}$=0.

However, galaxies in general may have bulge and disk components and, therefore, a large range in scale lengths. In order to enhance the light distribution analysis we utilize a second parameter: the concentration index (CI). We calculated the CI index as the ratio of the flux from the inner part of the galaxy to 1/3 of the flux from its outer annulus. The one-third factor brings the comparison to an equal-area basis, and makes it independent of the distance of the galaxy. The outer aperture was defined as the ellipse fitted to calculate the LD. The inner aperture was chosen as a smaller ellipse, half the size of the outer one. The annulus is the space between the inner and the outer apertures. As defined, CI can range between zero and infinity.

The two structural indices are similar to those used in Brosch *et al.* (1998), with the differences being: (a) the use of the $H\alpha$ flux instead of the number counts of HII

regions, (b) the application of an objective automatic algorithm instead of eyeball recognition, (c) the derivation of the full LD instead of only indices, and (d) the use of a normalization factor of 1/3 instead of 1/4 for CI. Another difference is that here we calculate the CI and AI indices for the continuum, as well as for the net line emission.

### 3.2. Results

In Fig. 3 we plot the structural indices vs. the number of HII regions and ellipticity of the ellipse contour. The number of HII regions in BCDs ranges from one to three, and for LSBs from one to twelve. These numbers represent the number of resolved peaks detected in the LDs by an automatic algorithm that searches for slope changes in the LDs. The main limitation of the algorithm is the lack of resolution in special cases of multiple HII regions perfectly aligned in the radial direction. Since the 'clumpiness' of a galaxy depends on the seeing, the resolution at which the image is sampled, and on the resolution of the LDs, we cannot derive the number of HII regions in real galaxies as an absolute parameter; for example, nearby systems will appear clumpier than more distant ones. We show below that a change in the resolution, or a difference in the number of HII regions between BCDs and LSBs, cannot explain the differences in concentration indices between the types. Due to the intrinsic irregular shape of these galaxies, the ellipticity (e=1 - b/a) is also uncertain, but it does provide some measure of the inclination. We can see in Fig. 3b and Fig. 3d that the derived quantities are not simply the result of projection effects or affected by extinction through the disk.

The profile of the lopsidedness distribution appears to be related to the central surface brightness of a galaxy. A characteristic feature of the low surface brightness (LSB) sub-group is the multi-component structure of the LD, with sharp features shown in the $H\alpha$ profiles, while the continuum LD is smoother and with shallower features (Figs. 2.1 through 2.3), but not fully symmetric. The multiplicity of the $\mathrm{AI}_{H\alpha}$ profiles

indicates that a number of individual HII regions with different luminosities and sizes are distributed over the galaxy; some may even not be resolved or recognized in our images but their contribution to the local H$\alpha$ flux is counted by the algorithm.

The interpretation of the LD profile widths depends not only on the sizes of the HII regions but also on their radial location; single HII regions closer to the center produce a wide peak, while those further out show narrow peaks. At the same radial distance, the bigger the size of the HII region, the wider the LD profile will appear. A nuclear HII region of some extent will present a flat profile. In the BCD sub-sample, many of the LDs show profiles that are mostly smooth, free of multi component structure, generally symmetric and wide (Figs. 1.1 through 1.3), as expected for single HII regions located near the centers. BCDs tend to be more concentrated than the LSBs; the median $CI_{H\alpha}$ is 8.56 for BCDs and 2.25 for the LSBs. We found a strong correlation between $\log(CI_{Cont})$ and $\log(CI_{H\alpha})$ (Fig. 4a) with the correlation coefficient cc=0.61 (F=36)[2]. Linear regression tests between other data sets are listed in Table 3. At the same CI, both sub-samples reach similar degrees of asymmetry. Note that both galaxy types tend to clump at $\log(CI_{Cont})=0.5\pm0.2$ and $A_{Cont}=0.2\pm0.1$ (Fig. 4c). The entire sample has a median $A_{H\alpha}$ of 0.69; the median for BCDs is 0.71 and for LSBs is 0.69.

We find an apparent upper limit for the asymmetry of the continuum light; 97% of the galaxies have $A_{Cont} \leq 0.5$ (Fig. 4c). We also find an apparent lower limit of the emission line asymmetry; 97% of the galaxies have $A_{H\alpha} \geq 0.3$ (Fig. 4d). A perusal of Tables 2.1, 2.2, and 2.3 shows that the *Cont* asymmetry is always smaller than the H$\alpha$ asymmetry. A $\chi^2$-test of the cumulative histograms of $A_{H\alpha}$ and $A_{Cont}$ indicates that

[2]F is the ratio between the mean square deviation due to the regression and the mean square deviation due to the residual variation. For a linear regression, which is the present situation, $F=t^2$ and this is the equivalent of a t-test. For more details see Draper & Smith (1981).

the two data sets originate from different distributions ($\chi^2$=244, with 18 degrees of freedom). The median *Cont* asymmetry is 0.25 for BCDs, 0.21 for LSBs, and 0.23 for all the objects with narrow-band images for the *Cont*. Note that objects with blue images for the continuum were not included in this analysis. Median values of the structure parameters are listed in Table 4.

A fundamental issue is whether the continuum and line-emission LDs are correlated in angular phase. We should expect a correlation if the locus of recent star formation, as witnessed by the H$\alpha$ emission, responds with a delay to some disturbance of the stellar distribution (the continuum light), producing a lag in the angular distribution of the azimuthal indices. This can be understood in a scenario of rotating disk-like systems. In fact, HI synthesis maps of a number these galaxies (Skillman *et al.* 1987; van Zee *et al.* 1997c, 1998a, b) show rotation-dominated systems with maximal rotation velocities of 40 – 100 km sec$^{-1}$ and with slowly rising rotation curves, typical of very late-type spirals (some appear to be undergoing small differential rotation), or systems with velocity still increasing beyond the optical disk, characteristic of the solid-body rotation found in many low-mass systems. In those cases, the angular phase correlation may depend on many factors, such as differences in the angular momentum of the stellar and gas masses, rotational speed, disk shear, and external SF triggers. Note that GR 8, Leo A and DDO 210 do not have well defined rotation curves (Carignan *et al.* 1990; Young & Lo 1996; Young, van Zee, & Lo 2000). The mismatch of the velocity gradient and the HI major axis in Leo A hints that some very low mass systems may be tumbling rather than spinning. In such cases, a delay between the past and the recent onset of star formation should also be expected.

To measure the correlation in the phase space of the line azimuthal asymmetry distribution with the distribution of the continuum light we used a similar analysis to that applied to the study of AGNs variability in the time-frequency domain

(Netzer *et al.* 1996; Kaspi *et al.* 2000). The technique is the derivation of the cross-correlation function (CCF), which is a set of correlation coefficients, giving a measure of the correlation between two data sets. We used here two methods: the first one is the discrete correlation function (DCF; Edelson & Krolik 1988), which we applied after interpolating 45 continous data points every 4°. The second method is the Z-transformed discrete correlation function (ZDCF) of Alexander (1997), which is an improvement of the DCF. For unevenly-sampled sets of data the ZDCF has the advantage that it avoids interpolation and reduces the resulting uncertaintly in the position of the peak. This is a consequence of the Fisher Z-transformation to the correlation coefficients and of the binning by equal population, rather than by equal separation.

The typical errors in the lags rage between $0.5 - 2°$, with the exception of 40° in IIZW40. The two methods (DCF and ZDCF) gave consistent results for our data, and we will refer to the ZDCF results in the following analyses. The uncertainties in the cross-correlation lags were conservatively over-estimated by the Monte Carlo-averaged ZDCF with simulated random errors and were provided by the ZDCF procedure of Alexander (1997). The results of the cross-correlation analysis are presented in Tables 2.1 and 2.2. The columns labeled "$r_{zdcf}$" show the peaks of the CCFs, defined as the point of maximum correlation; a high value of "$r_{zdcf}$" implies a good correlation between the two azimuthal indices at the listed "lag". For the definition of "$r_{zdcf}$" see Alexander (1997). The sign of the lag is defined as $AI_{Cont}$ - $AI_{H\alpha}$, that is $AI_{Cont}$ lags after $AI_{H\alpha}$.

The cross-correlation (CC) analysis of the H$\alpha$ vs. continuum distribution of AIs indicates a very high CC for a broad range of angular phase lags. The CC is higher for BCDs than for LSBs, and there is a trend for smaller angular phase lags in BCDs than in LSBs (Figs. 5a and 5b). In fact, $\sim 62\%$ of the BCDs having peak CC coefficient above 0.8 show lags smaller than $|\Delta\Phi| < 30°$ compared to $\sim 33\%$ of LSBs. The higher CC is explained by increased CIs (Fig. 5c), however the distribution of lags seems to be

independent of the concentration parameter (Fig. 5d).

## 4. A random distribution of star formation regions?

In this section we explore the possibility that the properties found for star-forming regions in dIs can be produced by random processes that engulfs the full scale of a galaxy. We tested a model of random star formation by constructing 1000 images of galaxies, which simulate the observed net H$\alpha$-flux and off-band red emission of dIs as found above, without distinguishing between LSB and BCD types. The model was created with the ARTDATA package in IRAF and included atmospheric seeing effects and detector readout noise.

A galaxy was modeled as a disk centered on a 256×256 pixel image with zero background. The intensity profile was that of an exponential disk $I = I_{\circ} exp(-1.6783R/R_{\circ})$, with the scale radius $R_{\circ}$ containing half the total flux. The apparent integrated magnitudes, scale-lengths, position angles of the major axis, and ellipticities were allowed to change randomly. The total magnitudes followed a Schechter (1976) luminosity function with $\alpha$=1.6 and $M_{\star} = -21.41$ in the red continuum, covering the apparent magnitude range from 17 to 19, similar to that of the objects in our sample. The maximum semi-major axis at half-flux was set to 30 pixels. The ellipticity was allowed to vary between 0.05 and 1.00. Random noise was added to the image by using Poisson statistics; a similar process was followed for the net and continuum images described below. At this stage, the output parameters of the disk were recorded as an ellipse contour with a semi-major axis twice the derived scale length. That is, $\mathrm{CI}_{Cont} = 3$ and $\mathrm{A}_{Cont} = 0$, by the definition of the underlying exponential disk.

The $H\alpha$ emission image was created by random generation of coordinates of up to 15 objects within the ellipse derived from the disk on a mean zero background. This range

(1-15) covers the number of resolved peaks detected in the LDs with the algorithm, as explained before. We will show that changing the total resolution, or the ratio between maximum and minimum resolution, cannot explain the differences in concentration indices between BCDs and LSBs. The objects simulate HII regions, whose apparent magnitudes were allowed to change randomly between 18 and 23 following a shallow power law with index 0.1. This range of magnitudes reproduces the $H\alpha$ flux densities observed for the HII regions of our sample of galaxies and yields total line fluxes in the range $10^{-15}$ - $10^{-13}$ erg cm$^{-2}$ s$^{-1}$. We assumed a simplified profile for an individual HII cloud as a spherical distribution with a star-like Moffat profile ($\beta$ =2.5). A Moffat profile (Moffat 1969) appears more natural than a Gaussian, because it produces a sharper boundary to an HII region, as expected for a Strömgren sphere. However, this choice does not appear to affect the results described below.

The red continuum image was simulated by adding to the smooth underlying exponential disk the same list of objects coordinates and flux densities that represented the HII regions, but this time simulating red star clusters (or super star clusters) distributed on the disk. Keeping the same distribution (with zero angular phase lag) implies an a-priori correlation of HII regions with the red star clusters restricted to zero angular phase lag. Keeping the same flux densities implies a uniform equivalent width (EW) for all individual HII regions, limited to the FWHM of the narrow filters used for the observed galaxies, that is 50 - 89Å . This assumption is justified by our finding for dIs in the Virgo Cluster where we showed that individuals HII regions are restricted to EW=10 to 100Å (Heller *et al.* 1998). We found that, in this way, the images and the LD profiles of the simulated net and continuum images reproduced the patterns observed in the real images. The simulation results in high degrees of star formation lopsidedness with a median $A_{H\alpha} = 0.77$, for $CI_{H\alpha}$ ranging from 0.01 to 30 (median $CI_{H\alpha} = 1.05$). A comparison set of net H$\alpha$ and continuum images, as well as plots of the azimuthal asymmetry of a real galaxy and a simulated one is shown in Fig. 6.

We plot in Fig. 7 the dependence of $A_{H\alpha}$ and $CI_{H\alpha}$ of the simulated galaxies on the number of HII regions (N) and on the integrated H$\alpha$ fluxes. The results show no dependence on the total flux. Changing N does not affect the lopsidedness range of possibilities, but there is a clear trend to $CI_{H\alpha}$=1 as the number of HII regions increases. This effect is reflected in Figure 8 where we plot $A_{H\alpha}$ vs. $\log(CI_{H\alpha})$ for all simulated galaxies (filled circles). Note that these galaxies are distributed around $CI_{H\alpha}$=1. The actual galaxies (represented by triangles and squares) show, in general, higher values of $CI_{H\alpha}$ than the simulated galaxies.

A closer look at the plots of $A_{H\alpha}$ vs. $\log(CI_{H\alpha})$ for different number of HII regions (Fig. 9) helps us interpret this effect. We see that the "phase space" accessible to simulated galaxies in the AI-CI plane becomes more restricted, the more HII regions a galaxy has. While for N=1 objects almost one half of the plane is populated, at N=12 the distribution is concentrated mostly at $CI_{H\alpha}$=1 for a large spread of AI's.

A trend of reduced concentration with increasing number of HII regions is visible for the right side of the distribution in Fig. 9. This is explained as the result of the fact that the more HII regions a (simulated) galaxy has, the more "balanced" is the distribution of these HII regions. Another trend is visible for the left side of the distribution in Fig. 9. The fewer HII regions a galaxy has, the better the chance to find these "unbalanced", more to one side of a galaxy than the other. This means that galaxies with few HII regions will be more asymmetric than galaxies with many HII regions. A test for 15-20 HII regions did not change the distribution for N=12, but it is obvious that by increasing N it will finally converge to the point ($A_{H\alpha}$=0, $CI_{H\alpha}$=1).

In order to test if the number of HII regions of the actual galaxies was exaggerated by the number of irregularities detected in the LDs we plotted in Fig. 10 only simulated galaxies with N=1, 2 and 3. We can see that reducing the number of HII regions shifts the simulated galaxies to a higher mean $CI_{H\alpha}$=1.3. This fits better the LSB sub-group,

however, it is not enough in order to explain the general shift of the BCD galaxies. We discuss this in the next section.

Summarizing, we have shown how the degree of asymmetry and concentration index of star forming regions in simulated galaxies change with the total number of HII regions and their luminosity distribution. A similar asymmetry behaviour occurs for the continuum, but to a lesser degree, due to the relatively smaller contribution of the young stellar clusters over the disk brightness.

## 5. Discussion

Our analysis indicates that most dIs show a lopsided morphology in their recent star formation and in the distribution of red light. Since the analysis was performed on the basis of structural indices that are independent of distance, angular size, and/or inclination of the galaxies, we believe that this is a intrinsic property of dwarf-irregular galaxies. The entire sample has a median lopsidedness index of 0.69 in their star forming distribution; similar results are obtained for LSBs and BCDs. For the same concentration index, LSB and BCD galaxies reach similar degrees of lopsidedness. The correlation detected between the continuum and the line emission concentration is supported by a strong correlation between on-going star formation regions and the red stellar population in the angular-phase domain. The correlation is stronger in BCDs, with a trend for smaller angular phase lags than LSBs. The results are consistent with the correlation found between line and continuum fluxes of individual HII regions in dIs in the Virgo Cluster, which is much stronger for BCDs than for LSBs (Heller *et al.* 1999).

We mentioned already an important difference between the BCD and LSB galaxies: BCDs exhibit stronger H$\alpha$ concentration in their nuclear regions than do LSBs. This is emphasized by the profiles of the lopsidedness distribution and is best seen in the

distribution of $CI_{H\alpha}$ (see e.g., Fig. 4a), where the squares tend more to the right than the filled triangles. This tendency is not shown as strongly in the distribution of $CI_{Cont}$; the degree of concentration of the red continuum light in BCDs is rather similar to that in LSB galaxies (Fig. 4c).

Interpreting the continuum light in the simulated galaxies as showing the distribution of previous stellar generations implies that in this aspect LSBs and BCDs are similar, but it is clear that shorter scale-length exponential disks are needed in compact galaxies. The implication is the presence of at least one past major star formation event in the central regions. This result is consistent with detailed surface brightness fitting of BCDs (e.g., Salzer & Norton 1998, Norton & Salzer 2000).

The differences become more evident as one compares the distribution of newly-formed stars, as measured by the H$\alpha$ emission in the real galaxies, with that in the simulated galaxies. BCDs have more concentrated emission and do not fit the median $CI_{H\alpha}$ of the simulated galaxies. The different concentration indices measured for the two types are not merely a result of fewer HII regions per BCD than per LSB; reducing to 1-3 the number of HII regions in simulated galaxies increased the mean of the distribution by 30%, but the lower limit in $CI_{H\alpha}$ for BCDs stayed were the model predicts the mean. We conclude that randomly generated star formation may be proceeding through the disk in LSB dwarf-irregular galaxies, but probably not in BCDs.

The higher correlation of the line and continuum LDs in BCDs is reminiscent of the similarity of blue and near-IR images of galaxies in the HDF (Richard Ellis, private communication). In the rest frame of these galaxies, imaged with the WFPC-2 and NICMOS, the optical colors correspond to rest-frame UV (i.e., the young stars) and the near-IR correspond to the optical continuum light used here to estimate the distribution of the older stellar populations. Their correlation shows that at z $\approx$2 the young stars form where there are more of the old stars, as we found here for dwarf irregulars.

From the diagram in Fig. 10 we learn that there is a limit to the degree of concentration a real LSB galaxy can have; higher CI indices would imply non-realistic, extremely extended galaxies with a dominant optical core, such as the very rare Malin I-types. In our LSB sample, the upper concentration limit is set by the extended-HI galaxy sub-group of van Zee *et al.* (primary). The behavior should be similar at the lower limit, but this limit is not well-defined.

## 6. Conclusions

We analyzed images of 78 dIs and measured the concentration and asymmetry of the H$\alpha$ line and red continuum emission by applying an objective automatic algorithm and by tracing the asymmetry along the azimuthal direction. Our findings show a high degree of asymmetry of the H$\alpha$ emission, which follows a milder asymmetry in the distribution of the red light. Both concentration indices (line and continuum) are highly correlated. The continuum and line emission lopsidedness distribution are correlated in angular phase, and there is a trend for higher correlation and smaller angular phase lags in BCDs than in LSBs. We found considerable differences between these two types of dwarf galaxies in terms of lopsidedness distribution profiles and concentration index.

We showed that a random distribution of HII regions can produce the observed lopsidedness of low surface brightness disk-like systems. The key parameters that most affect the model are the scale lengths, the number of HII regions per galaxy, and the luminosity distribution of the HII regions. The model fits well most of the observables: the frequency, strength, and profiles of the lopsidedness are recovered, both in the line emission and in the continuum. The model matches the distribution observed in normal LSB dwarf galaxies in the lopsidedness-concentration plane, but short scale-length exponential disks and some central diffuse light components are called for in LSB galaxies with extended HI envelopes. We showed that reducing the number of HII regions cannot

explain the higher concentrations observed in BCDs. It seems that a random distribution of star formation may explain the patterns observed in LSB dIs, but not in BCDs.

## Acknowledgments

AH and NB acknowledge support from the US-Israel Binational Science Foundation. EA is supported by a special grant from the Ministry of Science and the Arts to develop TAUVEX, a UV space imaging experiment. NB is grateful for the continued support of the Austrian Friends of Tel Aviv University. Astronomical research at Tel Aviv University is partly supported by a Center of Excellence Award from the Israel Academy of Sciences.

## References

Abraham, R. G., van den Bergh, S., Glazebrook, K., Ellis, R. S., Santiago, B. X., Surma, P., & Griffiths, R. E., 1996, ApJS, 107, 1.

Alexander, T., in "Astronomical Time Series", edited by D. Maoz, A. Sternberg & E. M Leibowitz, 1997, Astrophysics and Space Science Library, 218, Kluwer: Dordrecht.

Almoznino, E. & Brosch, N., 1998, MNRAS, 298, 920.

Brosch, N., Heller, A.B. & Almoznino, E., 1998, MNRAS, 300,1091.

Carignan, C., Beaulieu, S., & Freeman, K. C., 1990, AJ, 99, 178.

Conselice, C. J., 1997, PASP, 109, 1251.

Conselice, C. J. & Bershady, M.A., in "After the Dark Ages: When Galaxies were Young (the Universe at $2 < z < 5$).", 9th Annual October Astrophysics Conference

in Maryland, held 12-14 October,1998. , edited by S. Holt & E. Smith., American Institute of Physics Press, 1999, 225.

Dohm-Palmer, R. C., Skillman, E. D., Saha, A., Tolstoy, E., Mateo, M., Gallagher, J., Hoessel., J., Chiosi, C., Dufour, R. J., 1997, AJ, 114, 2527.

Dohm-Palmer, R. C., Skillman, E. D., Saha, A., Tolstoy, E., Mateo, M., Gallagher, J., Hoessel., J., Chiosi, C., Dufour, R. J., 1998a, AJ, 115, 152.

Dohm-Palmer, R. C., Skillman, Gallagher, J., Tolstoy, E., Mateo, M., Dufour, R. J., Saha, A., Hoessel., J., Chiosi, C., 1998b, AJ, 116, 1227.

Draper, N.R. & Smith, H., 1981, *Applied Regression Analysis*, New York: Wiley, 32.

Edelson, R., & Krolik, J. H., 1988, ApJ, 333, 646.

Elmegreen, B. G., 1998, in "Origins of Galaxies, Star, Planets and Life" (C. E. Woodward, H. A. Thronson & M. Shull, eds.), ASP series.

Gerola, H., Seiden, P. E., Schulman, L., S., 1980, ApJ, 242, 517.

Heller, A. B., Almoznino, E. & Brosch, N. 1998, IAU Colloquium No. 171: "The Low Surface Brightness Universe", ed. J. I. Davies, C. Impey, & S. Phillips, ASP Conf. Series, 170, 282.

Heller, A. B., Almoznino, E. & Brosch, N., 1999, MNRAS, 304, 8.

Heller, A. B., Almoznino, E. & Brosch, N., 2000, in preparation.

Hunter, D. A., Elmegreen, B. G., & Baker, A. L., 1998, ApJ, 493, 595.

Jog, C. J., 1997, ApJ, 488, 642.

Kaspi, S., Smith, P. S., Netzer, H., Maoz, D., Jannuzi, B. T., & Giveon, U., 2000, ApJ, in press.

Kornreich, D. A., Haynes, M. P., & Lovelace, R. V. E., 1998, AJ, 116, 2154.

Larson, R. B., 1986, MNRAS, 218, 409.

Leitherer, C. & Heckman T.M., 1995, ApJS. 96, 9.

Levine, S. E. & Sparke, L.S., 1998, ApJ, 496L, 13L.

Netzer, A., Heller, A., Loinger, F., Alexander, T., Baldwin, J. A., Wills, B. J., Han, M., Frueh, M., & Higdon, J. L., 1996, MNRAS, 279, 429.

Mihos, J. C., McGaugh, S. S., & de Blok, W. J. G., 1997, AA, 477, L79.

Moffat, A. F. J., 1969, A& A, 3, 455.

Norton, S. A. & Salzer, J. J., 2000, in preparation.

Rudnick, G. & Rix. H.W., 1998, AJ, 116, 1163.

Salzer, J. J. & Norton, S.A., 1998, IAU Colloquium No. 171: "The Low Surface Brightness Universe", ed. J. I. Davies, C. Impey, & S. Phillips, ASP Conf. Series, 170, 253.

Schechter, 1976, ApJ, 203, 297.

Skillman, E. D., Bothun, G. D., Murray, M. A., & Warmels, R.H., 1987, A&A , 185, 61.

van Zee, L., Haynes, M. P., & Salzer, J. J., 1997a, AJ, 114, 2479.

van Zee, L., Haynes, M. P., & Salzer, J. J., 1997b, AJ, 114, 2497.

van Zee, L., Haynes, M. P., Salzer, J. J., & Broeils, A. H., 1997c, AJ, 113, 1618.

van Zee, L., Westpfahl, D., Haynes, M. P., Salzer, J. J., 1998a, AJ, 115,1000.

van Zee, L., Skillman, E. D., & Salzer, J. J., 1998b, AJ, 116,1186.

Walker, I. R., Mihos, J. C. & Hernquist, L. , 1996, ApJ, 460, 121.

Young, L. M., Lo, K. Y., 1996, ApJ, 462, 203.

Young, L. M., van Zee, L., & Lo, K. Y., 2000, in preparation.

Zaritsky, D. & Rix. H. W., 1997, ApJ, 477, 118.

| BCD GALAXIES | | | | | LSB GALAXIES | | | | |
|---|---|---|---|---|---|---|---|---|---|
| Object | Ref. | a | e | PA | Object | Ref. | a | e | PA |
| MK 5 | 5 | 19 | 0.48 | 10 | VCC 17 | 1 | 46 | 0.47 | -60 |
| MK 36 | 5 | 10 | 0.25 | -34 | VCC 169 | 1 | 20 | 0.28 | 60 |
| MK 324 | 5 | 12 | 0.10 | -7 | VCC 217 | 1 | 56 | 0.67 | -90 |
| MK 328 | 5 | 13 | 0.15 | 49 | VCC 260 | 1 | 27 | 0.20 | -30 |
| MK 475 | 5 | 9 | 0.22 | -79 | VCC 328 | 1 | 33 | 0.55 | 20 |
| MK 600 | 5 | 26 | 0.39 | -51 | VCC 350 | 1 | 19 | 0.65 | -60 |
| MK 750 | 5 | 17 | 0.48 | 51 | VCC 477 | 1 | 27. | 0.04 | 40 |
| MK 900 | 5 | 24 | 0.25 | 19 | VCC 530 | 1 | 41 | 0.20 | -80 |
| UM 40 | 5 | 9 | 0.46 | 10 | VCC 826 | 1 | 59 | 0.43 | -40 |
| UM 133 | 5 | 26 | 0.75 | 22 | VCC 963 | 1 | 37. | 0.05 | -80 |
| UM 323 | 5 | 15 | 0.18 | -57 | VCC 1455 | 1 | 23 | 0.43 | -80 |
| UM 408 | 5 | 8 | 0.12 | -80 | VCC 1465 | 1 | 25. | 0.30 | 10 |
| UM 439 | 5 | 19 | 0.47 | -24 | VCC 1468 | 1 | 28 | 0.41 | 5 |
| UM 461 | 5 | 9 | 0.20 | 80 | VCC 1585 | 1 | 41 | 0.50 | -90 |
| UM 462 | 5 | 13 | 0.33 | 63 | VCC 1753 | 1 | 16 | 0.22 | -20 |
| I ZW 18 | 5* | 7 | 0.36 | -42 | VCC 1952 | 1 | 22 | 0.45 | -20 |
| II ZW 40 | 5* | 34 | 0.35 | -50 | VCC 1992 | 1 | 26 | 0.23 | -20 |
| WAS 5 | 5 | 9 | 0.25 | -77 | UGC 191 | 3 | 48 | 0.40 | -20 |
| VCC 10 | 7 | 23 | 0.50 | -4 | UGC 634 | 3 | 48 | 0.50 | 38 |
| VCC 144 | 7 | 13 | 0.30 | -30 | UGC 891 | 3 | 41 | 0.70 | 59 |
| VCC 172 | 7 | 27 | 0.57 | -20 | UGC 1175 | 3 | 23 | 0.30 | -42 |
| VCC 324 | 7 | 29 | 0.22 | 32 | UGC 2162 | 3 | 27 | 0.50 | -53 |
| VCC 410 | 7 | 9 | 0.25 | -35 | UGC 3050 | 3 | 21 | 0.20 | -10 |
| VCC 459 | 7 | 22 | 0.46 | 38 | UGC 4762 | 3 | 25 | 0.60 | 15 |
| VCC 513 | 7 | 13 | 0.16 | 44 | UGC 5364 (LEO A) | 2 | 138 | 0.40 | -86 |
| VCC 562 | 7 | 11 | 0.30 | 53 | UGC 5764 | 3 | 41 | 0.60 | 51 |
| VCC 802 | 6 | 22 | 0.56 | 70 | UGC 7300 | 3 | 41 | 0.50 | -48 |
| VCC 985 | 7 | 13 | 0.47 | 74 | UGC 7949 (DDO 147) | 2 | 55 | 0.49 | 61 |
| VCC 1179 | 7 | 18 | 0.48 | 20 | UGC 8091 (GR 8) | 2 | 41 | 0.60 | 47 |
| VCC 1374 | 7 | 32 | 0.64 | -16 | UGC 9128 | 3 | 41 | 0.40 | 30 |
| VCC 1725 | 7 | 27 | 0.57 | -62 | UGC 300 | 4+ | 43 | 0.02 | -49 |
| VCC 1791 | 7 | 36 | 0.70 | 63 | UGC 521 | 4+ | 34 | 0.33 | 39 |
| VCC 2037 | 6* | 32 | 0.50 | 9 | UGC 2684 | 4+ | 69 | 0.72 | -70 |
| | | | | | UGC 2984 | 4+* | 62 | 0.20 | -6 |
| | | | | | UGC 3174 | 4+ | 34 | 0.30 | -84 |
| | | | | | UGC 3672 | 4+ | 48 | 0.70 | -48 |
| | | | | | UGC 4660 | 4+ | 48 | 0.21 | -40 |
| | | | | | UGC 5716 | 4+ | 62 | 0.45 | -9 |
| | | | | | UGC 7178 | 4+ | 62 | 0.34 | -71 |
| | | | | | UGCA 357 | 4+ | 89 | 0.70 | -12 |
| | | | | | HARO 43 | 4+ | 26 | 0.60 | -44 |
| | | | | | UGC 9762 | 4+ | 48 | 0.34 | 70 |
| | | | | | UGC 10281 | 4+ | 50 | 0.49 | 33 |
| | | | | | UGC 11820 | 4+ | 96 | 0.40 | -50 |
| | | | | | DDO 210 | 4+ | 69 | 0.60 | -85 |

| No. | Group | Reference | Galaxies |
|---|---|---|---|
| 1 | LSB | Heller *et al.* 1999 | 17 |
| 2 | LSB | Norton & Salzer 2000 | 3 |
| 3 | LSB | van Zee 1997a,b, secondary | 10 |
| 4 | LSB | van Zee 1997a,b, primary | 15 |
| 5 | BCD | Norton & Salzer 2000 | 18 |
| 6 | BCD | Heller *et al.* 2000 | 2 |
| 7 | BCD | Almoznino & Brosch 1998 | 13 |
| | | Total number of images | 78 |

Table 1: Sample of galaxies.

---

Note. — The various symbols are:

a = semi-major axis in arc seconds.

$e = 1 - \frac{b}{a}$ ellipticity of aperture.

PA = position angle in degrees, measured counter-clockwise from +y.

(*) certain/or probably interacting galaxies.

(+) objects with B–band images for the continuum.

BCD GALAXIES

| | *Cont* | | | | *Hα* | | | | | |
|---|---|---|---|---|---|---|---|---|---|---|
| Object | <AI> | ampl | CI | A | <AI> | ampl | CI | A | lag | $r_{zdcf}$ |
| MK 5 | 0.82 | 0.14 | 2.3 | 0.27 | 0.15 | 0.46 | 4.5 | 0.97 | 27 | 0.90 |
| MK 36 | 0.77 | 0.18 | 4.5 | 0.36 | 0.80 | 0.14 | 6.2 | 0.28 | -4 | 0.91 |
| MK 324 | 0.93 | 0.07 | 9.0 | 0.13 | 0.80 | 0.16 | 12.4 | 0.33 | -8 | 0.98 |
| MK 328 | 0.91 | 0.06 | 6.8 | 0.13 | 0.76 | 0.18 | 16.3 | 0.36 | 103 | 0.99 |
| MK 475 | 0.79 | 0.12 | 3.7 | 0.26 | 0.36 | 0.40 | 8.4 | 0.84 | -8 | 0.98 |
| MK 600 | 0.80 | 0.14 | 7.7 | 0.28 | 0.61 | 0.23 | 34.0 | 0.47 | -52 | 0.93 |
| MK 750 | 0.71 | 0.22 | 6.3 | 0.44 | 0.34 | 0.41 | 36.3 | 0.85 | 4 | 0.92 |
| MK 900 | 0.96 | 0.03 | 7.2 | 0.06 | 0.52 | 0.30 | 53. | 0.62 | 70 | 0.98 |
| UM 40 | 0.91 | 0.06 | 4.1 | 0.13 | 0.47 | 0.37 | 5.5 | 0.73 | 13 | 0.98 |
| UM 133 | 0.76 | 0.13 | 1.8 | 0.27 | 0.17 | 0.37 | 0.7 | 0.92 | -3 | 0.87 |
| UM 323 | 0.75 | 0.19 | 8.6 | 0.37 | 0.7 | 0.22 | 9.9 | 0.45 | -8 | 0.99 |
| UM 408 | 0.79 | 0.17 | 7.5 | 0.34 | 0.57 | 0.30 | 21.6 | 0.61 | 4 | 0.97 |
| UM 439 | 0.97 | 0.04 | 3.0 | 0.07 | 0.5 | 0.25 | 3.2 | 0.54 | -49 | 0.76 |
| UM 461 | 0.88 | 0.13 | 3.4 | 0.26 | 0.31 | 0.37 | 14.3 | 0.79 | 46 | 0.93 |
| UM 462 | 0.96 | 0.05 | 0.5 | 0.11 | 0.83 | 0.19 | 6.4 | 0.38 | 20 | 0.73 |
| I ZW 18 | 0.66 | 0.22 | 1.7 | 0.43 | 0.79 | 0.15 | 16.7 | 0.31 | -9 | 0.89 |
| II ZW 40 | 0.86 | 0.11 | 4.0 | 0.23 | 0.27 | 0.40 | 0.7 | 0.85 | -86 | 0.68 |
| WAS 5 | 0.85 | 0.12 | 3.6 | 0.25 | 0.44 | 0.36 | 25.9 | 0.75 | 0 | 0.97 |
| VCC 10 | 0.47 | 0.35 | 4.3 | 0.71 | 0.37 | 0.39 | 8.7 | 0.79 | -9 | 0.98 |
| VCC 144 | 0.89 | 0.08 | 4.6 | 0.16 | 0.71 | 0.19 | 7.3 | 0.38 | 60 | 0.99 |
| VCC 172 | 0.93 | 0.08 | 3.5 | 0.16 | 0.42 | 0.46 | 1.9 | 0.93 | 74 | 0.88 |
| VCC 324 | 0.75 | 0.19 | 4.1 | 0.38 | 0.62 | 0.28 | 30.2 | 0.55 | 8 | 0.98 |
| VCC 410 | 0.85 | 0.14 | 2.9 | 0.28 | 0.65 | 0.23 | 5.3 | 0.47 | -102 | 0.93 |
| VCC 459 | 0.82 | 0.18 | 8.5 | 0.36 | 0.35 | 0.45 | 3.2 | 0.92 | -18 | 0.91 |
| VCC 513 | 0.83 | 0.12 | 4.7 | 0.24 | 0.44 | 0.36 | 21.2 | 0.74 | 45 | 0.99 |
| VCC 562 | 0.78 | 0.14 | 8.0 | 0.29 | 0.77 | 0.20 | 4.9 | 0.39 | 33 | 0.92 |
| VCC 802 | 0.76 | 0.15 | 2.0 | 0.31 | 0.24 | 0.48 | 2.1 | 0.96 | -9 | 0.98 |
| VCC 985 | 0.85 | 0.11 | 2.3 | 0.23 | 0.65 | 0.32 | 2.3 | 0.65 | -105 | 0.97 |
| VCC 1179 | 0.84 | 0.11 | 2.5 | 0.22 | 0.47 | 0.29 | 4.4 | 0.71 | -45 | 0.93 |
| VCC 1374 | 0.86 | 0.09 | 3.0 | 0.18 | 0.38 | 0.37 | 3.8 | 0.75 | 8 | 0.90 |
| VCC 1725 | 0.90 | 0.09 | 1.8 | 0.18 | 0.45 | 0.34 | 1.9 | 0.71 | -40 | 0.79 |
| VCC 1791 | 0.91 | 0.11 | 2.3 | 0.21 | 0.65 | 0.27 | 2.3 | 0.56 | 8 | 0.88 |
| VCC 2037 | 0.85 | 0.11 | 2.8 | 0.22 | 0.51 | 0.37 | 15.2 | 0.76 | -26 | 0.98 |

Table 2.1: Structural parameters for BCD galaxies in the sample.

---

Note. — The various symbols mean:

<AI>=$< \frac{flux_i}{flux_j} >$ mean asymmetry index.

ampl = $\frac{AI_{max}-AI_{min}}{2}$ asymmetry amplitude.

CI= $\frac{flux_{in}}{\frac{flux_{out}}{3}}$ concentration index.

A= $\frac{AI_{max}-AI_{min}}{AI_{max}}$ lopsidedness index.

$r_{zdcf}$ is the maximun cross-correlation-coefficient of $AI_{H\alpha}(\Phi)$ with $AI_{Cont}(\Phi)$ for $\Phi$=lag

LSB GALAXIES

| | *Cont* | | | | *Hα* | | | | | |
|---|---|---|---|---|---|---|---|---|---|---|
| Object | <AI> | ampl | CI | A | <AI> | ampl | CI | A | lag | $r_{zdcf}$ |
| VCC 17 | 0.67 | 0.24 | 3.5 | 0.48 | 0.56 | 0.26 | 0.2 | 0.58 | -121 | 0.99 |
| VCC 169 | 0.73 | 0.23 | 0.5 | 0.45 | 0.56 | 0.45 | 0.2 | 0.95 | -60 | 0.82 |
| VCC 217 | 0.80 | 0.16 | 2.2 | 0.33 | 0.67 | 0.26 | 0.4 | 0.54 | -79 | 0.56 |
| VCC 260 | 0.75 | 0.21 | 2.7 | 0.43 | 0.69 | 0.32 | 1.7 | 0.67 | -110 | 0.86 |
| VCC 328 | 0.82 | 0.13 | 3.3 | 0.26 | 0.85 | 0.15 | 7.7 | 0.30 | -36 | 0.75 |
| VCC 350 | 0.79 | 0.17 | 2.1 | 0.34 | 0.38 | 0.45 | 0.2 | 0.96 | 17 | 0.75 |
| VCC 477 | 0.87 | 0.13 | 1.9 | 0.26 | 0.22 | 0.48 | 0.1 | 0.99 | -92 | 0.71 |
| VCC 530 | 0.86 | 0.09 | 2.2 | 0.17 | 0.64 | 0.34 | 6.4 | 0.69 | -74 | 0.62 |
| VCC 826 | 0.95 | 0.04 | 4.1 | 0.08 | 0.40 | 0.35 | 13.1 | 0.71 | -36 | 0.81 |
| VCC 963 | 0.87 | 0.11 | 1.8 | 0.23 | 0.66 | 0.25 | 0.6 | 0.50 | 32 | 0.91 |
| VCC 1455 | 0.93 | 0.07 | 3.7 | 0.14 | 0.71 | 0.28 | 8.9 | 0.55 | -49 | 0.84 |
| VCC 1465 | 0.89 | 0.09 | 2.0 | 0.19 | 0.45 | 0.34 | 0.9 | 0.73 | 0 | 0.70 |
| VCC 1468 | 0.92 | 0.06 | 2.1 | 0.13 | 0.39 | 0.38 | 1.1 | 0.77 | -117 | 0.56 |
| VCC 1585 | 0.96 | 0.07 | 3.5 | 0.14 | 0.36 | 0.41 | 1.7 | 0.85 | 54 | 0.61 |
| VCC 1753 | 0.83 | 0.13 | 2.6 | 0.27 | 0.48 | 0.38 | 1.2 | 0.77 | -12 | 0.96 |
| VCC 1952 | 0.78 | 0.17 | 6.2 | 0.35 | 0.56 | 0.32 | 6.7 | 0.65 | 35 | 0.92 |
| VCC 1992 | 0.88 | 0.13 | 1.7 | 0.25 | 0.57 | 0.41 | 1.1 | 0.83 | -70 | 0.99 |
| UGC 191 | 0.91 | 0.06 | 1.2 | 0.13 | 0.54 | 0.37 | 0.5 | 0.77 | 48 | 0.93 |
| UGC 634 | 0.90 | 0.08 | 2.9 | 0.17 | 0.60 | 0.32 | 1.2 | 0.64 | 0 | 0.88 |
| UGC 891 | 0.96 | 0.04 | 1.9 | 0.09 | 0.72 | 0.20 | 1.8 | 0.41 | 8 | 0.69 |
| UGC 1175 | 0.82 | 0.14 | 3.3 | 0.28 | 0.44 | 0.45 | 2.6 | 0.92 | -97 | 0.89 |
| UGC 2162 | 0.86 | 0.11 | 1.4 | 0.23 | 0.48 | 0.33 | 0.8 | 0.70 | 76 | 0.85 |
| UGC 3050 | 0.96 | 0.05 | 3.1 | 0.11 | 0.69 | 0.22 | 3.4 | 0.45 | 137 | 0.92 |
| UGC 4762 | 0.85 | 0.10 | 3.2 | 0.20 | 0.70 | 0.39 | 0.7 | 0.77 | 2 | 0.77 |
| UGC 5364 (LEO A) | 0.81 | 0.09 | 1.2 | 0.19 | 0.93 | 0.05 | - | 0.09 | -8 | 0.79 |
| UGC 5764 | 0.92 | 0.05 | 4.7 | 0.10 | 0.55 | 0.33 | 6.0 | 0.68 | 73 | 0.86 |
| UGC 7300 | 0.92 | 0.05 | 2.5 | 0.17 | 0.49 | 0.40 | 1.0 | 0.81 | -116 | 0.98 |
| UGC 7949 (DDO 147) | 0.96 | 0.03 | 1.7 | 0.05 | 0.48 | 0.36 | 0.5 | 0.74 | -12 | 0.63 |
| UGC 8091 (GR 8) | 0.56 | 0.30 | 1.1 | 0.61 | 0.33 | 0.42 | 0.4 | 0.88 | 33 | 0.92 |
| UGC 9128 | 0.88 | 0.16 | 1.2 | 0.16 | 0.21 | 0.45 | 0.1 | 0.94 | 20 | 0.88 |

Table 2.2: Structural parameters for LSB galaxies with narrow-band $H\alpha$ images for the continuum distribution.

| LSB GALAXIES | | | | | | | | |
|---|---|---|---|---|---|---|---|---|
| | B | | | | $H\alpha$ | | | |
| Object | <AI> | ampl | CI | A | <AI> | ampl | CI | A |
| UGC 300 | 0.85 | 0.13 | 3.8 | 0.26 | 0.66 | 0.39 | 5.1 | 0.79 |
| UGC 521 | 0.87 | 0.12 | 13.5 | 0.23 | 0.89 | 0.11 | 14.9 | 0.22 |
| UGC 2684 | 0.86 | 0.10 | 3.7 | 0.19 | 0.60 | 0.34 | 3.6 | 0.70 |
| UGC 2984 | 0.89 | 0.13 | 4.4 | 0.28 | 0.75 | 0.19 | 3.6 | 0.39 |
| UGC 3174 | 0.83 | 0.13 | 2.3 | 0.26 | 0.67 | 0.33 | 2.7 | 0.68 |
| UGC 3672 | 0.80 | 0.18 | 2.3 | 0.39 | 0.75 | 0.27 | 3.0 | 0.54 |
| UGC 4660 | 0.78 | 0.05 | 2.8 | 0.12 | 0.77 | 0.27 | 3.8 | 0.54 |
| UGC 5716 | 0.93 | 0.08 | 4.5 | 0.17 | 0.47 | 0.35 | 10.0 | 0.74 |
| UGC 7178 | 0.91 | 0.06 | 3.5 | 0.11 | 0.60 | 0.34 | 5.1 | 0.69 |
| UGCA 357 | 0.84 | 0.11 | 4.7 | 0.21 | 0.63 | 0.26 | 3.0 | 0.54 |
| HARO 43 | 0.93 | 0.06 | 13.7 | 0.12 | 0.93 | 0.14 | 15.0 | 0.28 |
| UGC 9762 | 0.84 | 0.13 | 3.7 | 0.25 | 0.64 | 0.28 | 5.2 | 0.55 |
| UGC 10281 | 0.63 | 0.20 | 1.6 | 0.42 | 0.54 | 0.37 | 5.9 | 0.78 |
| UGC 11820 | 0.87 | 0.10 | 3.4 | 0.20 | 0.60 | 0.27 | 2.1 | 0.56 |
| DD0 210 | 0.83 | 0.12 | 1.3 | 0.25 | 0.87 | 0.08 | 2.3 | 0.17 |

Table 2.3: Structural parameters for LSB galaxies with B–band images for the continuum distribution.

| Var. 1 | Var. 2 | cc | F |
|---|---|---|---|
| $\log(\mathrm{CI}_{Cont})$ | $\log(\mathrm{CI}_{H\alpha})$ | 0.67 | 60 |
| $\mathrm{A}_{Cont}$ | $\mathrm{A}_{H\alpha}$ | 0.16 | 1.9 |
| $\mathrm{A}_{H\alpha}$ | $\log(\mathrm{CI}_{H\alpha})$ | -0.40 | 14 |
| $\mathrm{A}_{Cont}$ | $\log(\mathrm{CI}_{Cont})$ | -0.02 | 0.03 |

Table 3: Linear regression tests.

| Var. | BCD | LSB | BCD+LSB |
|---|---|---|---|
| $\mathrm{CI}_{H\alpha}$ | 8.56 | 2.25 | 4.23 |
| $\mathrm{CI}_{Cont}$ | 4.90 | 2.70 | 3.43 |
| $\mathrm{A}_{H\alpha}$ | 0.71 | 0.69 | 0.69 |
| $\mathrm{A}_{Cont}$ | 0.25 | 0.21 | 0.23 |

Table 4: Median values of the structure parameters.

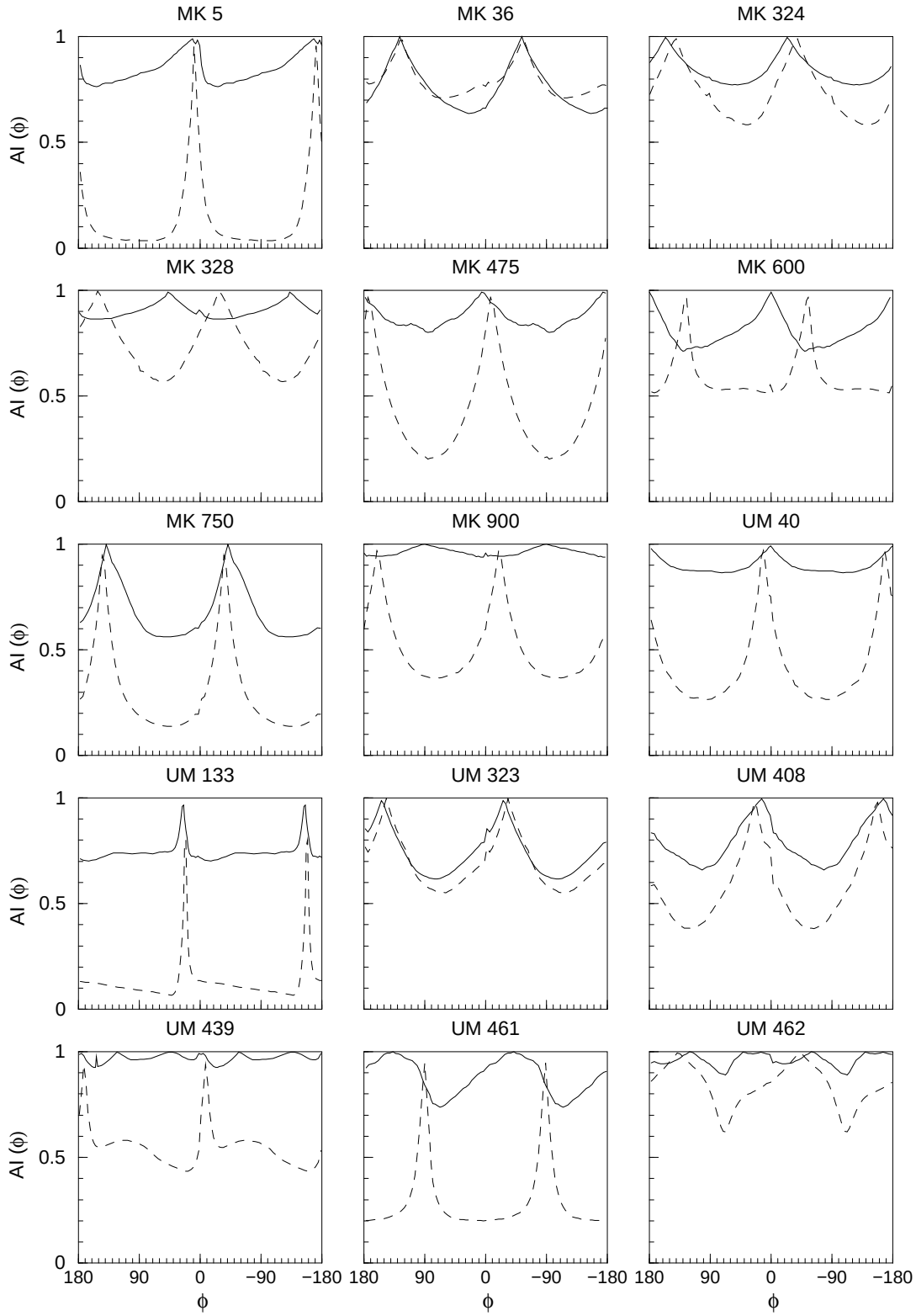


Fig. 1.1.— BCDs: Variation of AI vs. azimuthal angle ($\Phi$) measured anti-clockwise from North. *Cont* is plotted with a solid line and H$\alpha$ is plotted with a dashed line.

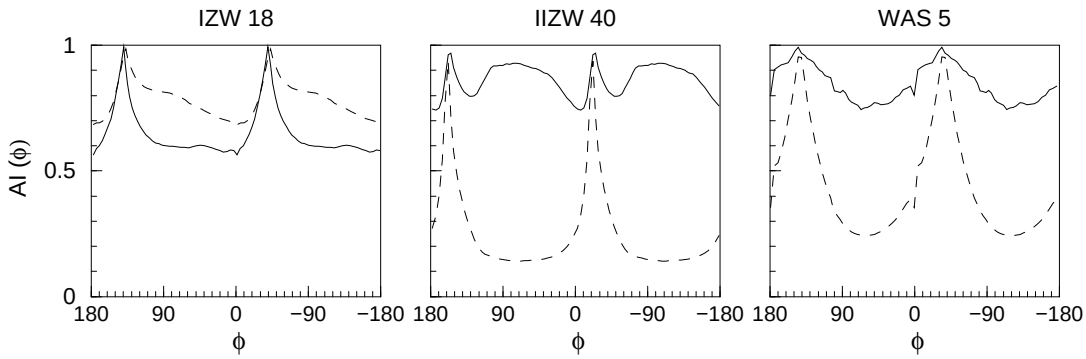


Fig. 1.2.— Same as Fig.1.1.

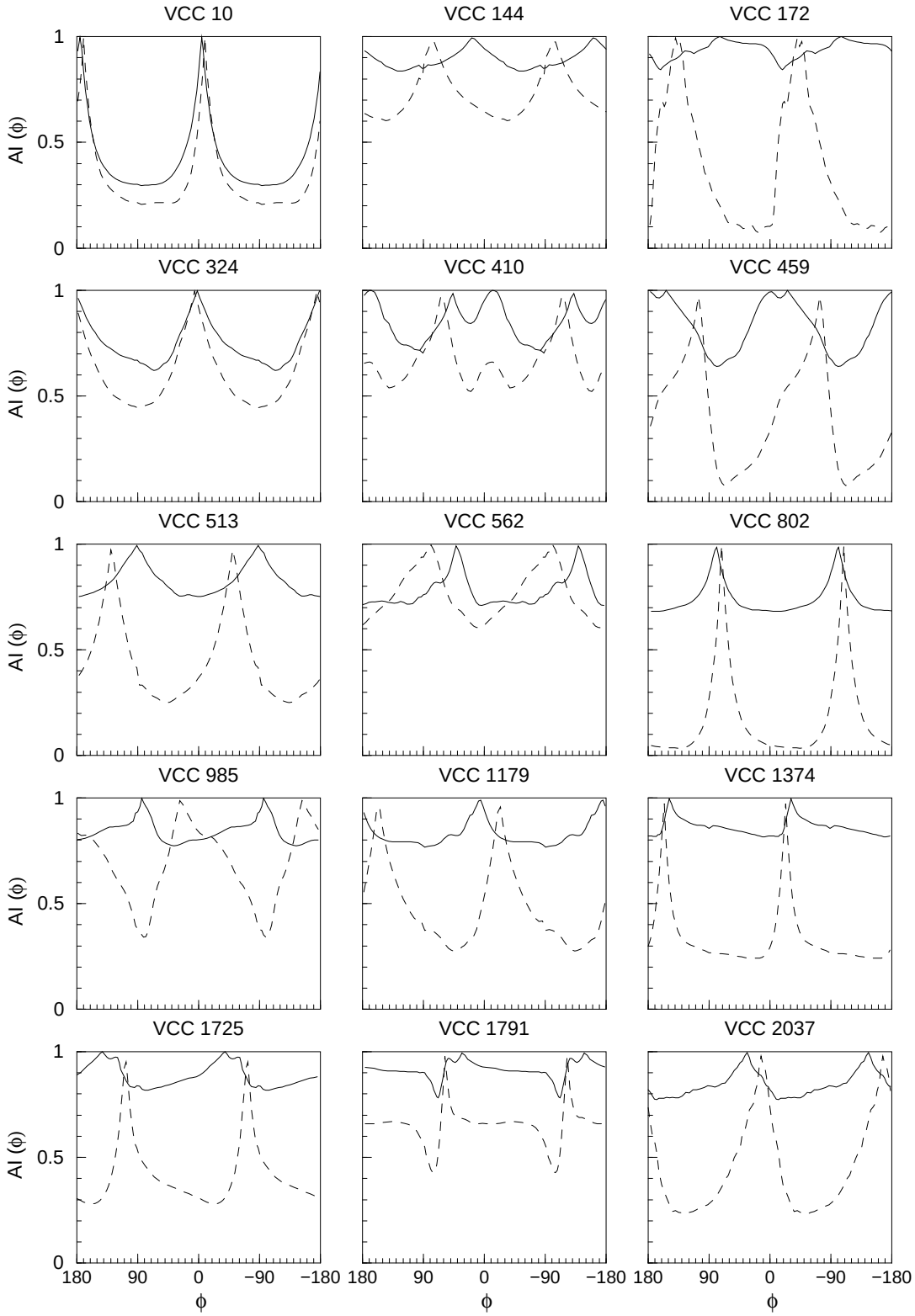


Fig. 1.3.— Same as Fig. 1.1.

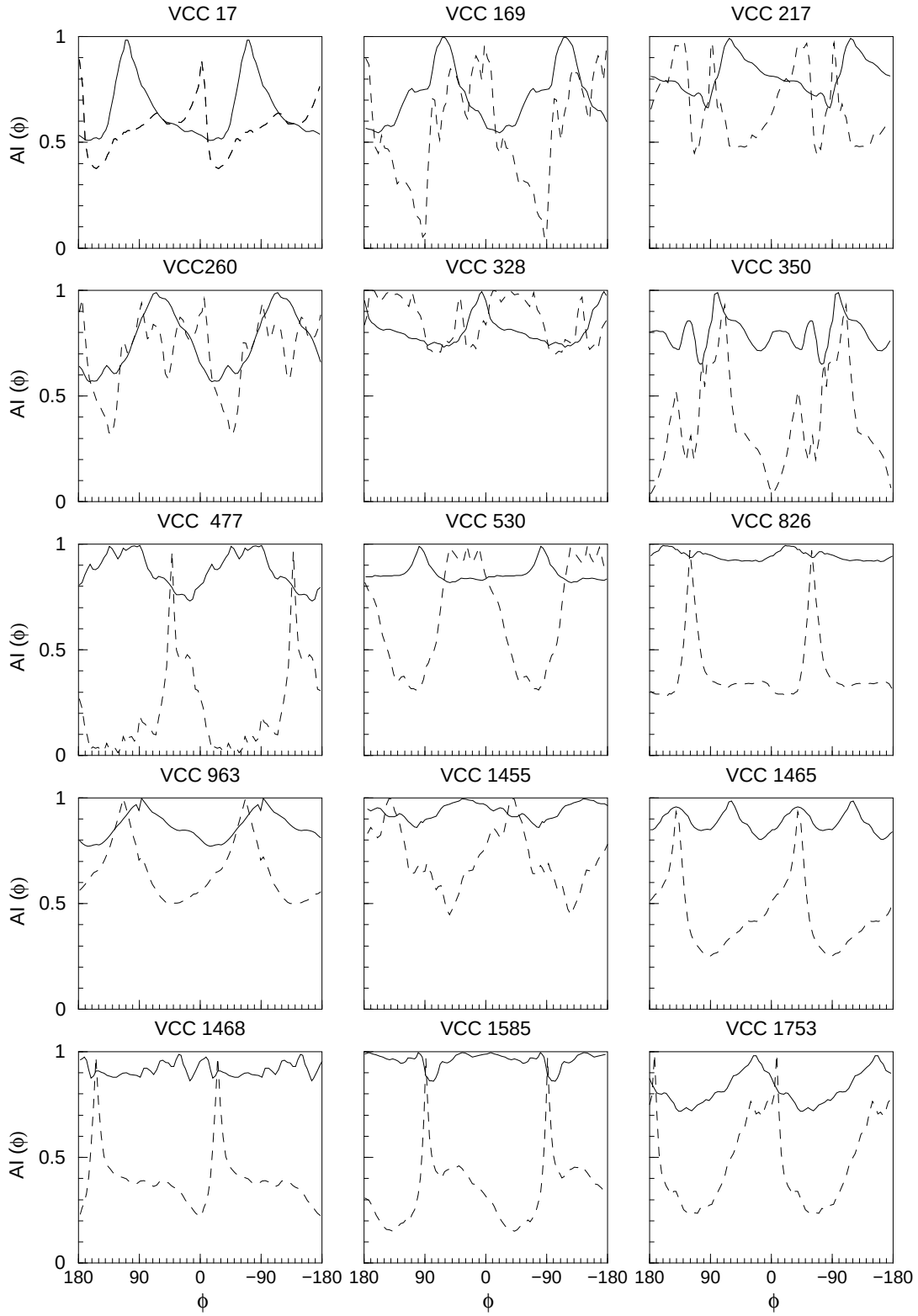


Fig. 2.1.— LSBs: Variation of AI vs. azimuthal angle ($\Phi$) for LSBs with narrow-band $H\alpha$ images for the continuum. *Cont* is plotted with a solid line and H$\alpha$ is plotted with a dashed line.

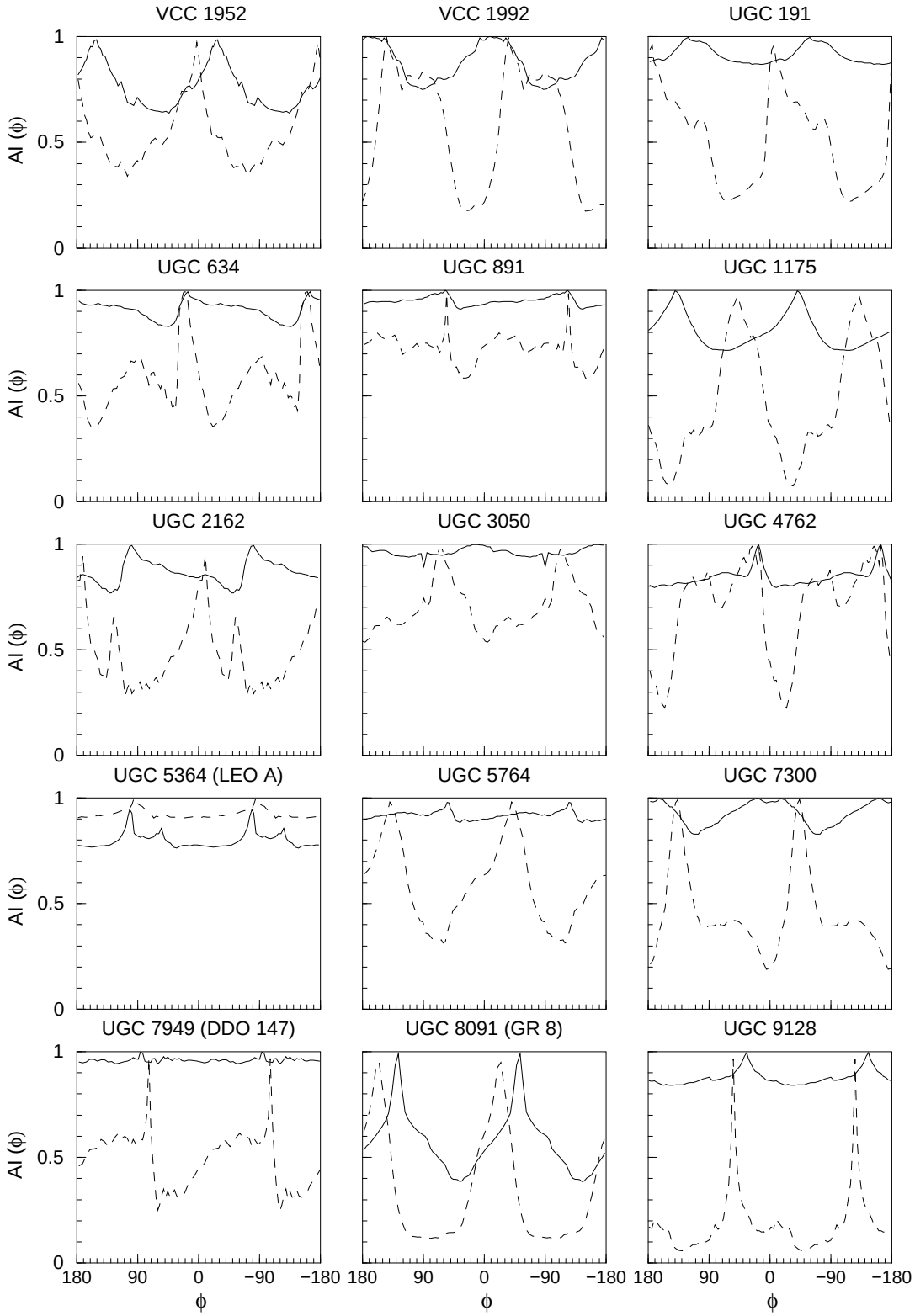


Fig. 2.2.— Same as Fig. 2.1.

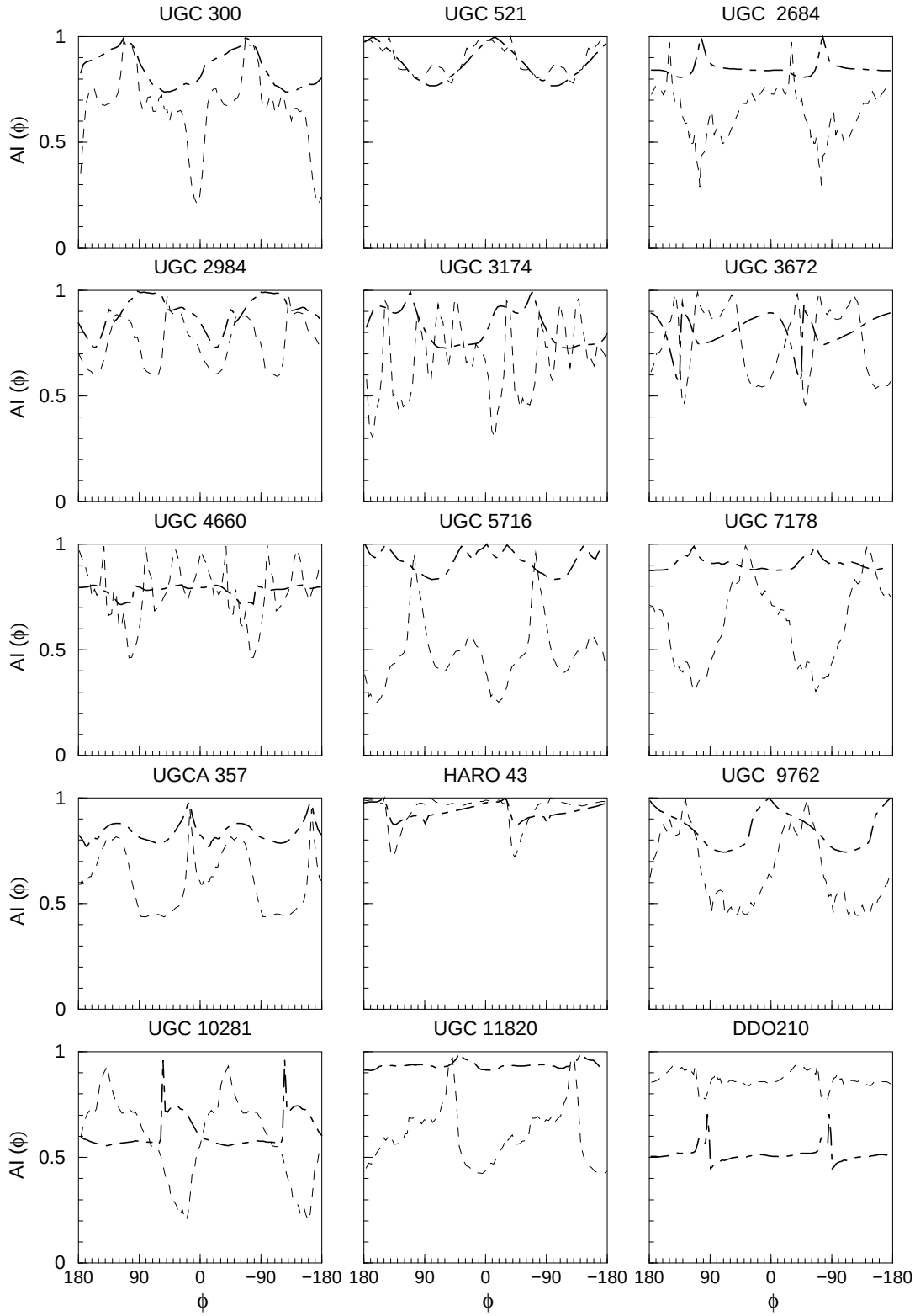


Fig. 2.3.— Variation of AI vs. azimuthal angle ($\Phi$) for LSBs with B–band images for the continuum. B–band is plotted with bold dot-dashed line and H$\alpha$ is plotted with a dashed line.

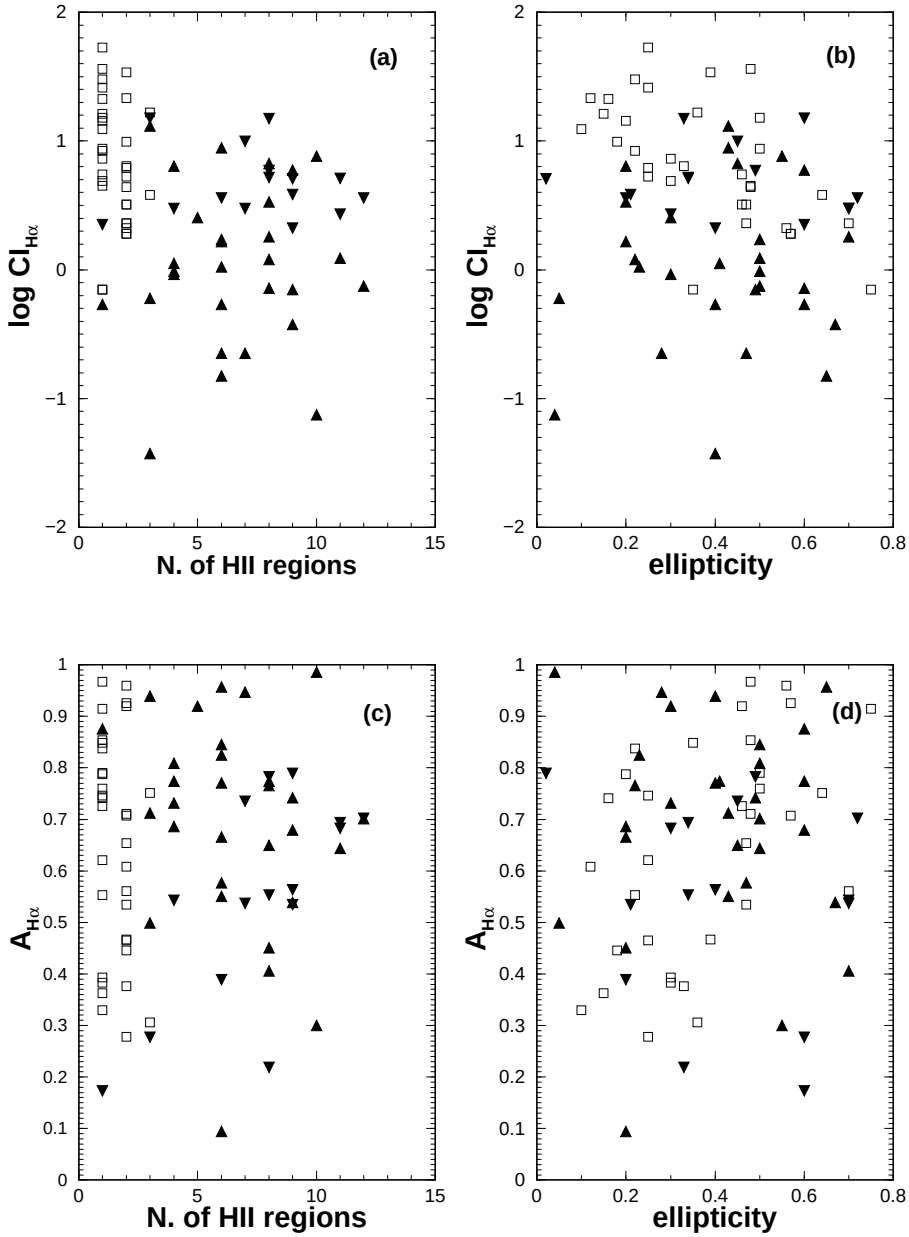


Fig. 3.— Observed galaxies: BCDs are represented by squares, LSBs are represented by triangles-up for objects with narrow-band $H\alpha$ images for $Cont$, and by triangles-down for objects with B-band images for $Cont$. The different panels show concentration index of $H\alpha$ flux vs. number of HII regions in (a), concentration index of $H\alpha$ flux vs. ellipticity in (b), lopsidedness vs. number of HII regions in (c), and lopsidedness vs. ellipticity in (d).

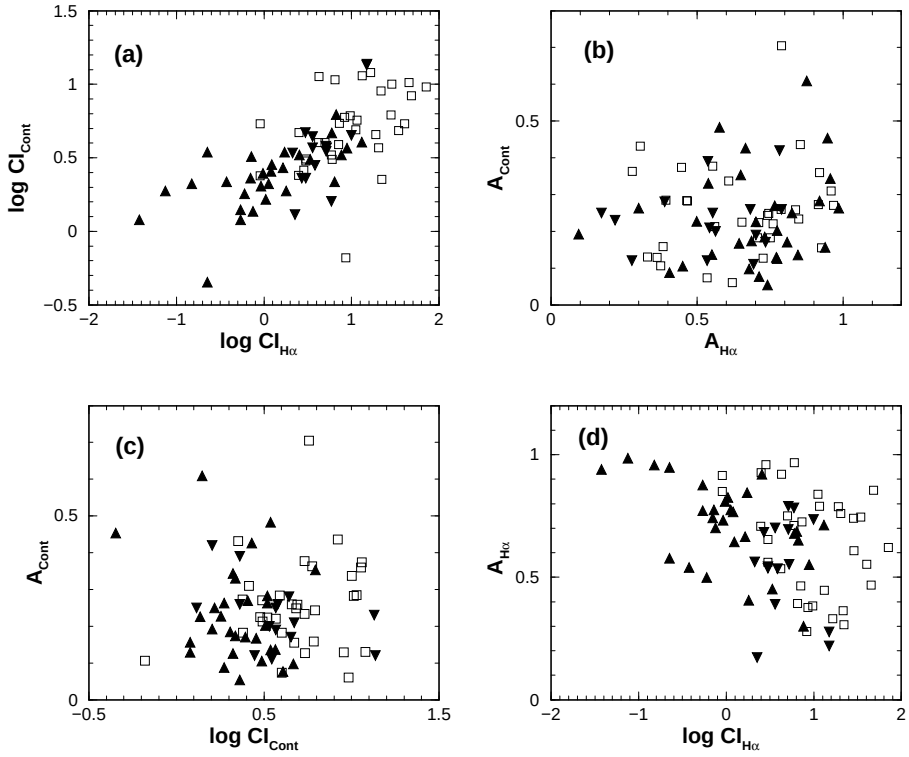


Fig. 4.— Correlations of parameters: the different panels show log $CI_{Cont}$ vs. log $CI_{H\alpha}$ in (a), $A_{Cont}$ vs. $A_{H\alpha}$ in (b), $A_{Cont}$ vs. log $CI_{Cont}$ in (c), and $A_{H\alpha}$ vs. log $CI_{H\alpha}$ in (d). Symbols as for Fig. 3.

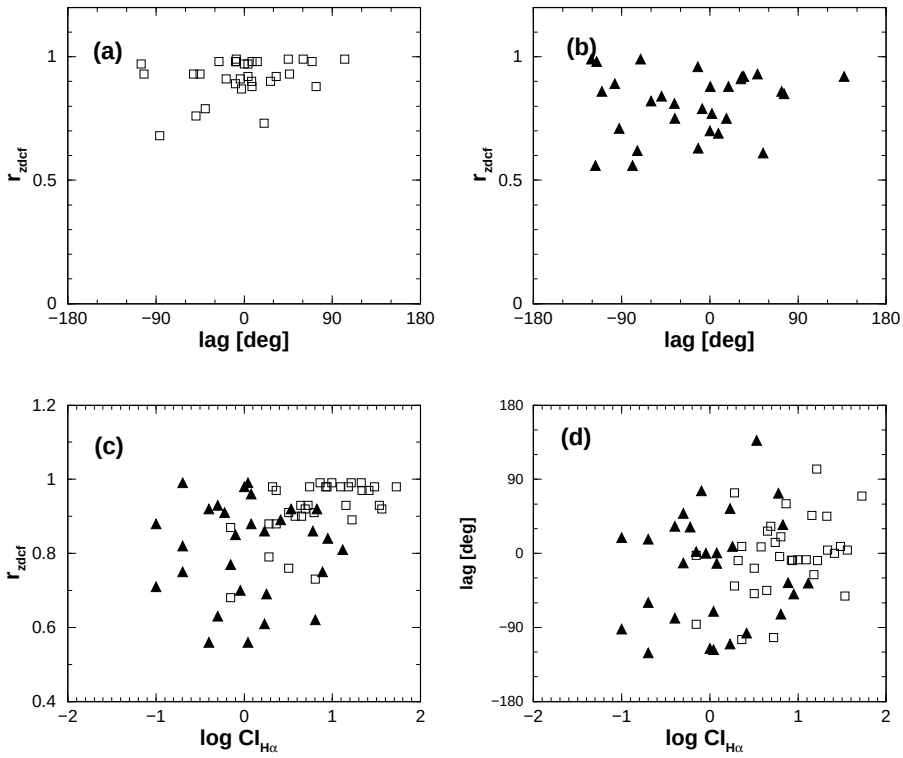


Fig. 5.— Maximum correlation coefficient $r_{zdcf}$ of $H\alpha$ vs. *Cont*, lag in degrees: BCDs in (a), LSBs in (b), $r_{zdcf}$ vs. log $CI_{H\alpha}$ in (c), lag vs. log $CI_{H\alpha}$ in (d). Symbols as for Fig. 3.

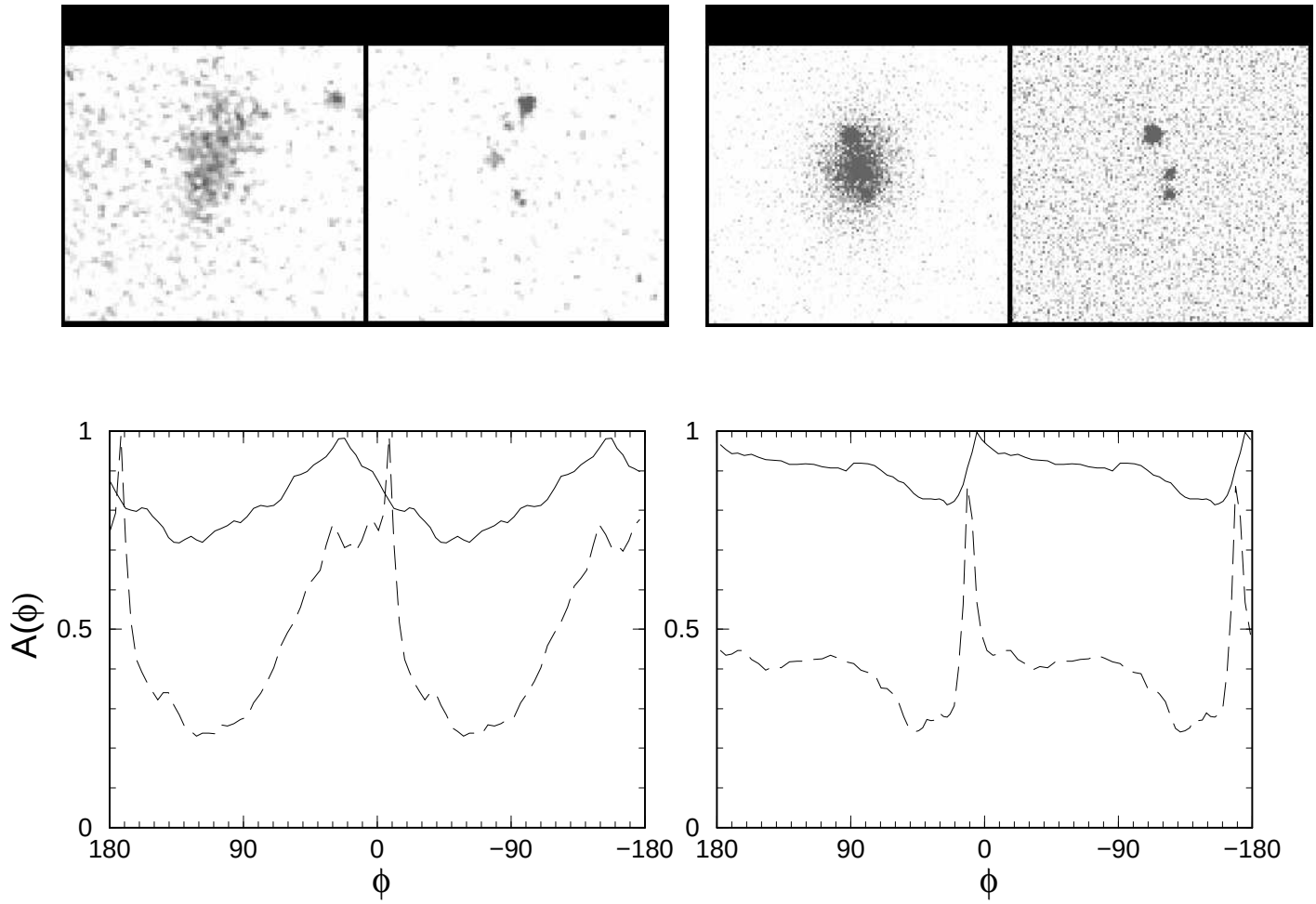


Fig. 6.— Comparison of a real galaxy (VCC1753) in the left part of the page and a simulated one in the right part. We show in the upper panels the continuum and H$\alpha$ images of both galaxies, and in the lower panels their azimuthal profiles.

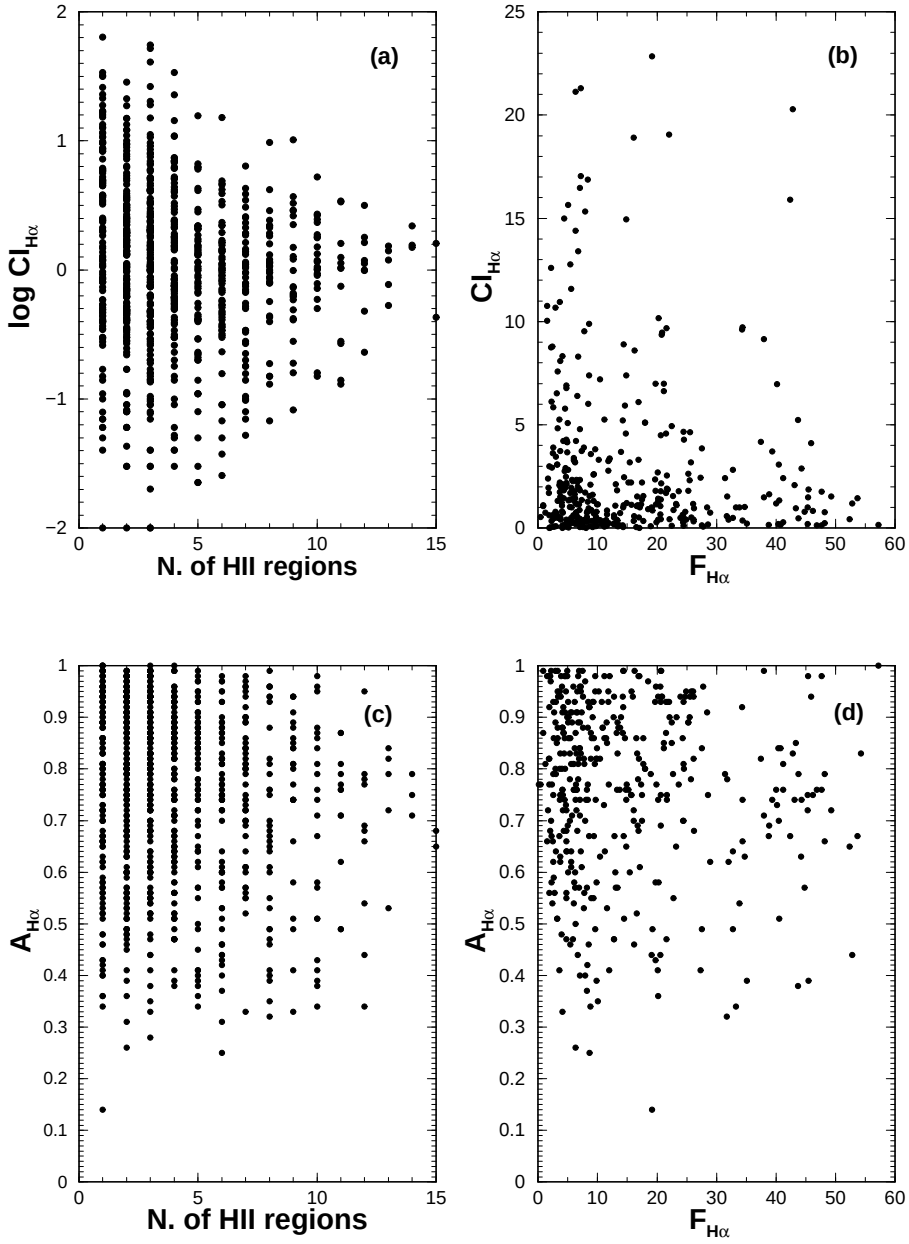


Fig. 7.— Artificial galaxies: (a) Concentration index of $H\alpha$ flux vs. number of HII regions, (b) Concentration index of $H\alpha$ flux vs. total $H\alpha$ flux, (c) Lopsidedness vs. number of HII regions, (d) Lopsidedness vs. total $H\alpha$ flux. The $H\alpha$ flux is in units of $10^{-14}$ erg cm$^{-2}$ s$^{-1}$

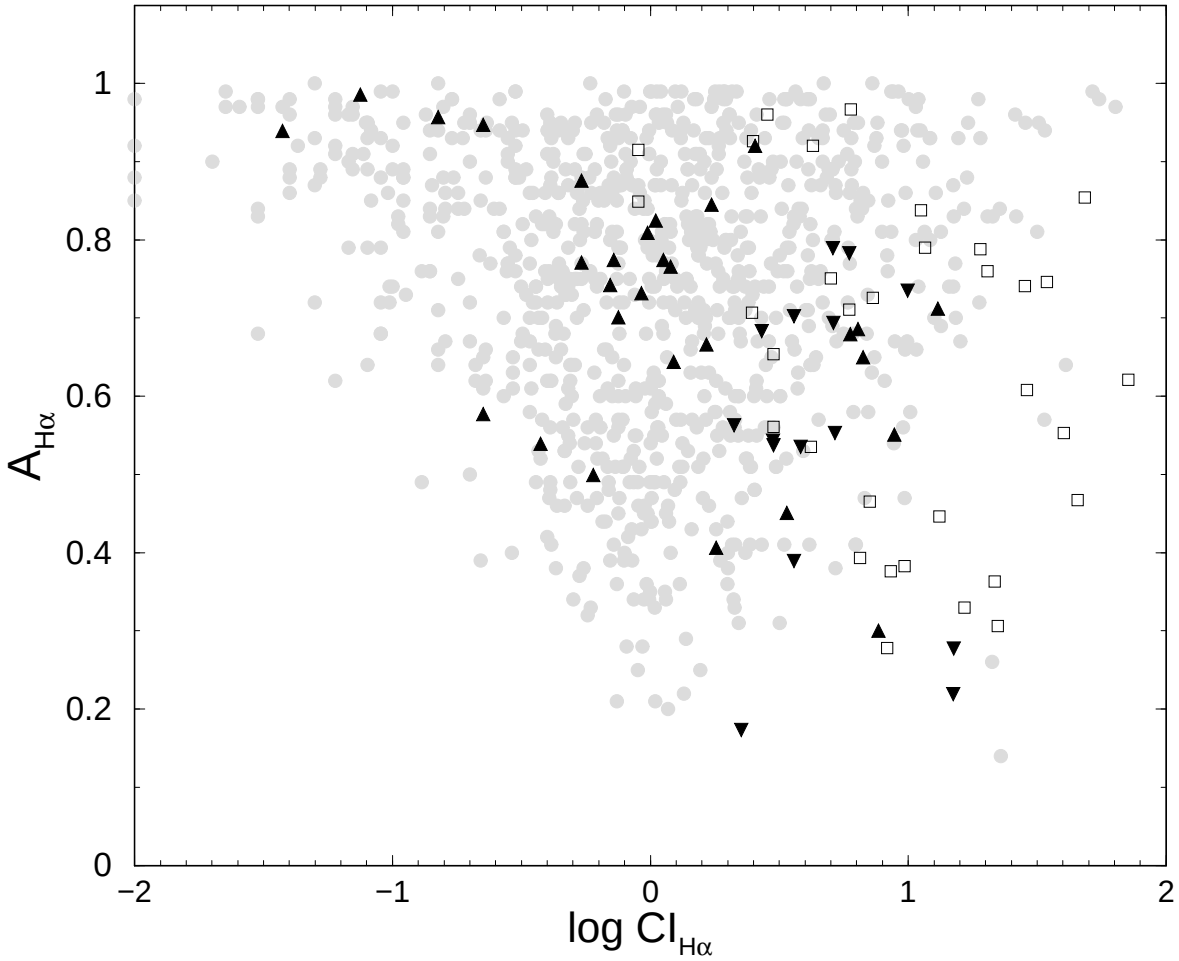


Fig. 8.— $A_{H\alpha}$ vs. $\log(CI_{H\alpha})$. Simulated galaxies with 1 to 12 HII regions are represented by circles, observed LSBs are represented by triangles-up for objects from Heller *et al.* 1999 and for van Zee *et al.* 1997a, b (secondary), triangles-down objects from van Zee *et al.* 1997a, b (primary), observed BCDs are represented by squares.

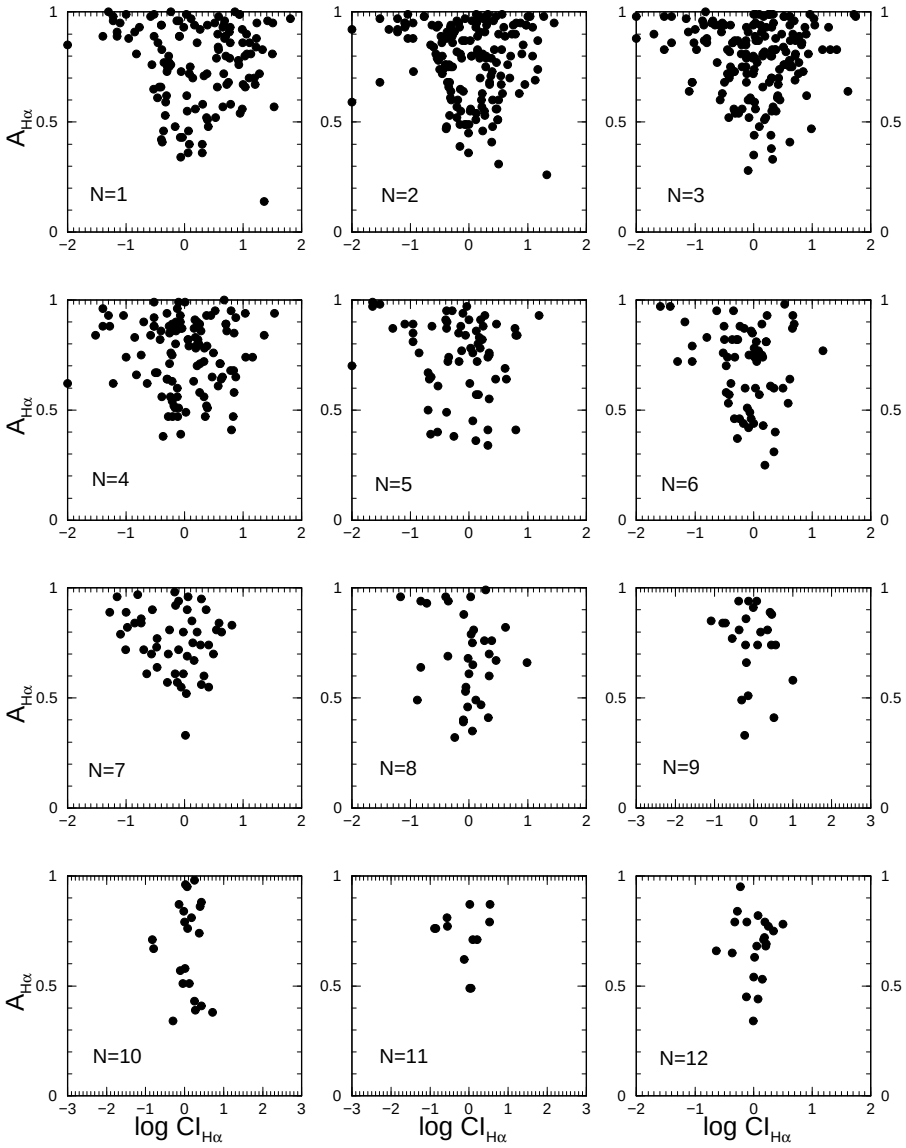


Fig. 9.— $A_{H\alpha}$ vs. $\log(CI_{H\alpha})$ for simulated galaxies, with 1 to 12 HII regions.

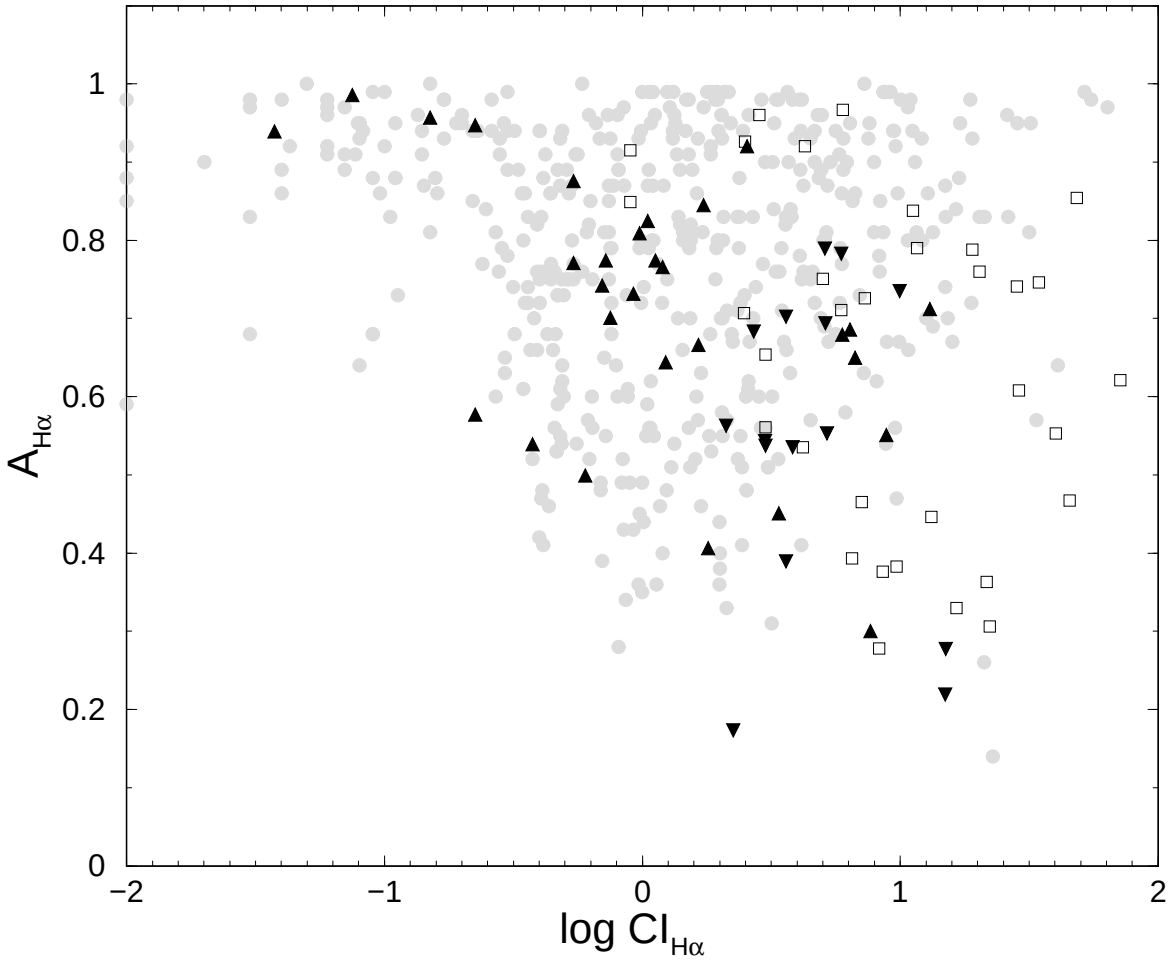


Fig. 10.— Same as Fig. 8 for simulated galaxies with 1 to 3 HII regions.